Using Icepack to reproduce Ice Mass Balance buoy observations in landfast ice: improvements from the mushy layer thermodynamics

Mathieu Plante[1], Jean-François Lemieux[1], L. Bruno Tremblay[2], Adrienne Tivy[3], Joey Angnatok[4], François Roy[1], Gregory Smith[1], Frédéric Dupont[5], and Adrian K. Turner[6]

[1]Recherche en prévision numérique environnementale, Environnement et Changement Climatique Canada, Dorval, Québec, Canada.
[2]Department of Atmospheric and Oceanic Sciences, McGill University, Montréal, Québec, Canada
[3]Canadian Ice Service, Environment and Climate Change Canada, Ottawa, Ontario, Canada.
[4]Nunatsiavut Research Center, Nain, Labrador, Canada.
[5]Service Météorologique Canadien, Environnement et Changement Climatique Canada, Dorval, Québec, Canada.
[6]T-3 Fluid Dynamics and Solid Mechanics Group, Theoretical Division, Los Alamos National Laboratory, Los Alamos, New-Mexico, USA

Correspondence: Mathieu Plante (mathieu.plante@ec.gc.ca)

Abstract.

Icepack v1.1.0–the column thermodynamics model of the Community Ice Code (CICE) version 6–is used to assess the impact of changing the thermodynamics from the Bitz and Lipscomb (1999) physics (hereafter BL99) to the mushy layer physics on the ability to reproduce in-situ landfast ice observations from two Ice Mass Balance (IMB) buoys co-deployed in a Fjord close to Nain (Labrador) in February 2017. To this end, a new automated surface retrieval algorithm is used to determine the in-situ ice thickness, snow depth, basal ice congelation and snow-ice formation from the measured vertical temperature profiles. Icepackv1.1.0 simulations are run to reproduce these observations using each thermodynamics schemes, with a particular interest on how the different physics influence the representation of snow-ice formation and ice congelation. Results show that the BL99 parameterization represents well the ice congelation but under-represents the snow-ice contribution to the ice mass balance. In particular, defining snow-ice formation based on the hydrostatic balance alone does not reproduce the negative freeboards observed for several days in the IMB data, resulting in a too early snow-ice formation, positive ice thickness bias and reduced snow depth variations. We find that the mushy layer thermodynamics with default parameters significantly degrades the model performance, overestimating both the congelation growth and snow-ice formation. The simulated thermodynamics response to flooding however better represents the observations, and the best results are obtained when allowing for negative freeboards in the mushy layer physics. The mushy thermodynamics also produces a larger variability in congelation rates at the ice bottom interface, alternating between periods of too-rapid ice growth and periods of unrealistic basal melt. This pattern is related to persistent brine dilution in the lowest ice layer by the congelation and brine drainage parameterizations. The mushy physics congelation is shown to come with significant frazil formation, which is not expected in a landfast ice context. This behaviour is attributed to the congelation parameterization not fully accounting for the conductive heat flux imbalance at the ice-ocean boundary. We propose a modification of the mushy layer congelation scheme that largely reduces the frazil formation and allows a tuning of the congelation rates to match the observations. Our results demonstrate that the mushy layer

physics and its parameters can be tuned to closely match the IMB observations, but that more observations are needed to better constrain them.

1 Introduction

25   The sea-ice and oceanography of the Canadian Arctic is largely modulated by the formation of landfast ice in fjords, along the coasts and in narrow channels. Each winter, this land-locked sea ice transforms the Canadian Arctic Archipelago (CAA) into a seasonal continent of stationary sea-ice (Melling, 2002; Galley et al., 2012), effectively insulating the sea-water from the cold atmosphere and barring the transport of ice through the CAA passages (Howell et al., 2013; Kwok, 2006). The landfast ice edge represents a seasonal boundary where the air-ocean exchanges and ice dynamics processes are concentrated, in particular

30   by the opening of semi-permanent polynyi under divergent surface forcing conditions (Melling et al., 2001; Dumont et al., 2010). These flaw polynyi in turn drive the regional meteorology (Barber et al., 2001; Gultepe et al., 2003; Lüpkes et al., 2008; Raddatz et al., 2011) and ocean circulation (Dumont et al., 2010), producing sediment-rich waters that are key to the Arctic marine ecosystem (Stirling, 1980, 1997; Carmack and Macdonald, 2002; Tremblay et al., 2002). As changes in the landfast ice cover are expected to alter these processes, its monitoring, representation in forecast models and inclusion in climate projections

35   are a concern not only for the study of the Arctic climate but also for a wide range of socio-economical aspects such as on-ice transport safety, food security and navigation planning (Gearheard et al., 2006; Eicken et al., 2011; Cooley et al., 2020).

In dynamical sea ice models, the physics of landfast ice is represented using a combination of thermodynamic relations governing the ice growth and melt (i.e., a column thermodynamics model, Maykut and Untersteiner, 1971; Semtner, 1976; Bitz and Lipscomb, 1999; Huwald et al., 2005; Turner et al., 2013) and of dynamical parameterizations governing its stability against

40   external forces (i.e. a rheological model, Hibler, 1979; Hunke and Dukowicz, 1997; Tremblay and Mysak, 1997; Wilchinsky and Feltham, 2004; Rampal et al., 2016). While these components are mostly treated (and developed) independently, they remain deeply inter-connected and the formation of landfast ice usually results from their combined action. In many areas, for instance, the landfast ice is held by the grounding of ice keels on the ocean floor, which involves prior ridging (dynamics) of sufficiently thick ice (thermodynamics). In the absence of ice grounding, landfast ice can form during periods of calm

45   and cold weather (Divine et al., 2004; Kirillov et al., 2021) during which leads freeze to a sufficient ice thickness for the unconsolidated ice floes to coalesce together (thermodynamics), allowing the formation of ice arches between pining points that resist subsequent surface forcings (dynamics, Dammann et al., 2019; Liu et al., 2022). In sea ice models, this inter-play between thermodynamic and dynamic factors is represented by ice thickness dependencies in the dynamical parameters, such as the seabed stress term (Lemieux et al., 2015) or the material strength parameters (Dumont et al., 2009; Lemieux et al.,

50   2016; Plante et al., 2020; Liu et al., 2022). The accurate representation of landfast ice extent, trends and variability in sea ice models therefore not only requires the permitting dynamics (i.e. ice grounding, tensile strength) but also thermodynamics that reproduces well the landfast ice growth and melt.

In the ECCC ice-ocean forecasting systems (e.g., RIOPSv2, Smith et al., 2021), the implementation of the aforementioned landfast ice dynamics was shown to greatly improve the representation of landfast ice in hindcast (free-run) simulations

(Lemieux et al., 2016). The timings of landfast ice formation and break up however remain difficult to reproduce, often off-set by a couple of weeks with respect to those recorded in operation ice charts (Lemieux et al., 2016). While this could be improved by modifications to the ice grounding mechanics (e.g., Dupont et al., 2022) or by changes to the ice strength formulation (Ungermann et al., 2017), it is also possible that the discrepancy is associated with a misrepresentation of the landfast ice thermodynamics, which in the ECCC systems is based on the model of Bitz and Lipscomb (1999, hereafter BL99). Thermodynamics models have grown in sophistication over the years, in particular with the representation of mushy layer physics (Feltham et al., 2006), brine dynamics (Notz and Worster, 2009; Turner et al., 2013) and melt ponds (Flocco et al., 2010; Holland et al., 2012; Hunke et al., 2013). These developments are implemented in the Los Alamos Community Ice CodE version 5 (CICE5) and were shown to have competing effects on the overall pan-Arctic ice mass balance, both in long-term global simulations (Turner and Hunke, 2015) and in coupled climate simulations (in the Community Earth System Model version 2, Bailey et al., 2020; DuVivier et al., 2021). The use of the mushy layer physics was in particular shown to produce larger amount of frazil and snow-ice, together increasing the overall ice thickness. Whether this increase is also seen in the landfast ice context (without sensitivities to the offshore sea-ice dynamics) remains to be determined.

In recent years, the deployment of Ice Mass Balance (hereafter IMB, used here as a general term, not referring to specific designs) buoys in both the Arctic and Antarctic provided in situ observations of the thermodynamics in the sea ice interior by measuring the internal sea ice temperature at high vertical (centimeters) and temporal (hours) resolution (Richter-Menge et al., 2006; Jackson et al., 2013; Planck et al., 2019). The snow depth and ice thickness conditions are inferred from the recorded vertical temperature profiles, traditionally by visual inspection (Tian et al., 2017; Provost et al., 2017) but more recently using automated algorithms (Liao et al., 2019; Cheng et al., 2020; Richter et al., 2023). These measurements give new insights on thermodynamic processes that are otherwise not detectable by traditional ice thickness measurements, ice core analysis or remote sensing, such as the formation of snow-ice (Provost et al., 2017; Rösel et al., 2018), heat fluxes within and between the material interfaces (Trodahl et al., 2000; West et al., 2020), brine convection and mushy layer properties (Wongpan et al., 2018). IMB buoys have also been used to assess the performance of thermodynamics models in the context of 1D simulations (Caixin et al., 2015; Tian et al., 2017; Duarte et al., 2020). The mushy layer physics in CICE version 5 for instance has been tested against IMBs deployed in the pack ice (first year and multi year) during the N-ICE2015 expedition North of Svalbard and was shown to adequately represent the observed sea ice growth but also to over-represent snow-flooding under large snow depth conditions (Duarte et al., 2020).

In this study, we investigate how updating the model thermodynamics from the BL99 to the mushy layer parameterization impacts the simulated sea ice mass balance in a landfast ice context, away from the pack-ice dynamics. This assessment is based on the in-situ observations from two IMB buoys that were deployed in a landfast ice channel well sheltered from offshore dynamics, close to Nain (Nunatsiavut, Labrador). A particular interest is placed on the ice growth from congelation and snow-ice formation, which is determined from the recorded internal temperature profiles using a novel surface retrieval algorithm building on the work of Liao et al. (2019); Cheng et al. (2020). Multiple Icepack (v1.1.0) model simulations are run to reproduce these observations using the BL99 physics or the mushy layer physics to determine the effect of the brine physics on the model performance. In particular, we find that the use of the mushy layer physics with default parameters significantly

degrades the model performance despite the improved representation of flooding and brine processes. The basal ice growth in mushy simulations is over-represented, includes a significant contribution from frazil production and exhibits unexpected periods of basal melt. The snow-ice formation is also over-represented due to early snow flooding when observations are under negative freeboard conditions. We show that these discrepancies are largely resolved by simple modifications and tuning of the congelation and snow-ice parameterizations. The contributions of this paper includes a modified mushy layer congelation parameterization not conducive to frazil formation, and a parameterized dependency of the snow flooding rates on negative freeboard values.

This manuscript is organised as follows. A description of the IMB buoys and surface forcing data used in the analysis is provided in section 2. The Icepack1.1.0 model physics is briefly presented in section 3, first describing the BL99 physics currently used in the ECCC forecast systems, then the differences when using the mushy layer thermodynamics. Our modifications to the snow-ice and congelation parameterizations are also included in this section. The methods are detailed in section 4, including the surface retrieval algorithm, the numerical simulation setup and model performance diagnostics. Results from the in-situ observations and Icepackv1.1.0 simulations are presented in section 5. Discussions on the model performance and conclusions are summarized in section 6.

2 Data

2.1 Ice mass balance buoy observations

Two Scottish Association for Marine Science (SAMS) Snow and Ice Mass Balance Apparatus (hereafter SIMBA) buoys were deployed in winter 2017 as part of an ongoing collaboration with the Nunatsiavut Research Center (NRC), with the goal of serving the Nain community with the deployment of scientific instruments in the local landfast ice. The buoys were thus not deployed as part of a wider scientific field observation campaign: the deployment dates and locations were chosen with NRC collaborators based on their sea ice monitoring interests. The first buoy (IMB1) was deployed on February 23rd, 2017 at $\sim 56.42°$ N, 61.7° W, in a landfast channel close to the southern coast of Satosoak island (see Fig. 1), and recovered two months later on April 18th. The second buoy (IMB2) was deployed during the same season on February 24th at $\sim 56.43°$ N, 61.50°W, ~ 12 km East of IMB1 in the same fjord close to Palungitak island, and recovered three months later on May 31st. To our knowledge, this was the first time IMB buoys were deployed in this area.

The SIMBA buoys consist of a 5 m long thermistor string with temperature sensors (Maxim DS28EA00, with 0.0625°C resolution and 0.0625°C accuracy) placed every 2 centimeters (Jackson et al., 2013). The thermistor strings are deployed vertically through a 5-cm hole such that the sensors measure the vertical temperature profile from the atmosphere above the snow layer down to the sea-water below the ice (Fig. 2a). At deployment, a section of the thermistor string is laid flat on the ice surface to mark the initial snow/ice interface in the data (see red arrows and dashed lines in Fig. 2a-b). The sensors within this thermistor string section are thus all at the same depth and show nearly identical temperature readings, making this segment easily identifiable in the vertical temperature profiles. The hole is then refilled with slush and the snow cover carefully restored

to its original depth. The vertical temperature profiles are measured with a 6-hour time resolution and are transmitted remotely via Iridium satellite along with the recorded air temperature, atmospheric pressure and GPS location.

The SIMBA also perform daily heat cycle measurements, which consist in recording the temperature change associated with a one- and two-minute heating from a resistor component besides each temperature sensor (Jackson et al., 2013). This change in temperature can be used to infer the heat capacity and conductivity of the medium surrounding the sensors, and is used in this study to visually locate the material interfaces and validate the accuracy of our surface retrieval algorithm.

2.2 GDPS atmospheric forcing

Data from the ECCC Global Deterministic Prediction System (GDPS, Buehner et al., 2015; Smith et al., 2018) is used to compute the atmospheric fluxes driving our thermodynamic simulations at the air-snow interface. The GDPS was previously shown to be equally representative of observations as more commonly used reanalysis data (Smith et al., 2014), and offers an accurate estimate of the atmospheric conditions in our study region with limited surface observations.

The GDPS is a coupled atmosphere-ice-ocean forecasting system using the Global Environment Multiscale (GEM) model for the atmosphere (Côté et al., 1998b, a), the Los Alamos multicategory Community Ice CodE (CICE) model version 4 for the sea ice (Hunke et al., 2010), and the Nucleus for European Modelling of the Ocean (NEMO) model for the ocean (Madec et al., 1998; Madec and the NEMO team, 2008). This system produces 10-day forecasts with 3-hourly outputs of the atmosphere, ice and ocean, initialized each day at 0000 UTC with fields from a data assimilation system (e.g., a four-dimensional ensemble-variational data assimilation scheme for the atmosphere, see Buehner et al., 2013, 2015, for details). Here, we use the archived surface fields from the 006-027h UTC forecasts (i.e., after a 6h spin-up) to drive the atmospheric fluxes in our model. At these very short lead times, only limited deviations from the initial analysis fields are expected (Smith et al., 2014). The GDPS variables used in our analysis include surface winds, air temperature, humidity, short and long wave radiations and precipitations, all taken at the grid point location closest to the buoy deployment.

3 Model

1D sea ice simulations are produced using Icepackv1.1.0, the thermodynamics package from CICE6. This package corresponds to a collection of thermodynamics parameterizations that can be chosen by the user. In this analysis, we use Icepack with two different thermodynamics schemes: simulations are first ran using the BL99 thermodynamics available in CICE version 4 and employed in the ECCC systems, and then repeated using the mushy layer thermodynamics, available from CICE version 5 onward. All simulations share the same surface energy balance (atmosphere and ocean fluxes) and snow model, but the mushy layer thermodynamics includes improvements in the representation of brine processes and modifications to the sea ice congelation and snow-ice formation parameterizations (Turner and Hunke, 2015; Bailey et al., 2020).

3.1 Standard BL99 thermodynamics

3.1.1 Surface thermodynamic balance

The thermodynamic growth and melt of sea ice are governed by the net energy balance at the top and bottom ice (or snow) surfaces. At the top interface, the atmospheric fluxes are calculated from the GDPS data and the net heat flux F_0 (positive downward) at the top interface is written as:

$$F_0 = F_s + F_l + F_{LW} + (1 - \alpha)(1 - i_0)F_{SW} \tag{1}$$

where F_s is the sensible heat flux, F_l is the latent heat flux, F_{LW} is the net long wave flux, α is the surface shortwave albedo, i_0 is the fraction of short wave penetration into the ice or snow surface and F_{SW} is the incoming shortwave flux. In all simulations, the shortwave albedo and penetration are defined by the Community Climate System Model version 3 (CCSM3, Collins et al., 2006).

Due to the absence of ocean salinity and currents observations at the buoy locations, no forcing data is used in our simulations to represent the oceanographic conditions. The ice-ocean fluxes are represented using the mixed layer parameterization included in Icepack v.1.1.0, which determines the Sea Surface Temperature (SST) and heat exchanges between the sea ice and the ocean based on a fixed mixed layer depth, Sea Surface Salinity (SSS) and skin friction velocity. Here, we set the SSS to 33 PSU (a value coherent with our measured ocean surface temperature of ∼-1.85 °C), the mixed layer depth to 20m (default value) and the skin friction velocity to 0.005 m s^{-1} (the set minimum in Icepack). The SST is prognostic but initialized at the freezing point (as calculated from the liquidus).

The net heat exchange F_{bot} between the ice and the ocean is given by:

$$F_{bot} = -\rho_w c_w c_h u_* (T_w - T_f), \tag{2}$$

where ρ_w (= 1026 kg/m^3) is the sea water density, c_w is the sea water specific heat capacity (= 4.218 kJ kg^{-1} K^{-1}), c_h (= 0.006) is a heat transfer coefficient, u_* is the ocean friction velocity (0.005 m s^{-1}) and T_w, T_f are the sea surface temperature and bottom ice temperature at freezing point. Note that when the SST is at freezing point, $T_w = T_f$ and $F_{bot} = 0$.

3.1.2 Enthalpy, temperature and salinity profiles

The vertical temperature profiles are computed with boundary conditions set from the surface energy balance described above. The temperature in the snow and ice interior layers is solved to satisfy a prognostic temperature equation, which treats sea ice as a single phased solid but represents brine via salinity dependencies in the heat conductivity and specific capacity definitions (see Bitz and Lipscomb, 1999, for details).

The top surface temperature T_{sf} is determined by the conductive flux needed to balance the net heat flux F_0:

$$F_0 = F_{ct} = K_{sf} \frac{2(T_{sf} - T_t)}{\Delta h_t}, \tag{3}$$

where F_{ct} is the top interface conductive flux, K_{sf} is the conductivity at the air-snow (or air-ice) interface, and T_t, Δh_t are the internal temperature and layer thickness of the top snow or ice layer. If $F_0 > 0$, T_{sf} is capped to the melting temperature and the remaining imbalance is used to melt snow or ice. At the ice bottom boundary, the temperature T_f is set to the freezing point of surface sea water.

The internal temperatures in each of the snow or ice layers are governed by the following prognostic equation:

$$\rho_i c_i \frac{\partial T_i}{\partial t} = \frac{\partial}{\partial z}\left(K_i \frac{\partial T_i}{\partial z}\right) - \frac{\partial}{\partial z}\left(I_{pen}(z)\right), \tag{4}$$

where ρ_i is the ice or snow density ($= 917$ kg/m^3 for sea ice, $\rho_s = 330$ kg/m^3 for snow), $c_i(T,S)$ is the specific heat of sea ice or snow, T_i is the internal temperature in the ice or snow layer, K_i is the thermal conductivity based on the Bubbly parameterization (Pringle et al., 2007), and $I_{pen}(z)$ is the flux of penetrating solar radiation at depth z according to Beer's law.

The enthalpy $q(T,S)$ of any interface or layer can be retrieved from the solved temperatures as follows:

$$q(T,S) = -\rho\left[c_0(T_m - T) + L_0\left(1 - \frac{T_m}{T}\right) - c_w T_m\right], \tag{5}$$

where S is the sea ice bulk salinity (fixed and based on observed vertical salinity profiles, Bitz and Lipscomb, 1999), c_0 ($= 2.106$ kJ kg^{-1} K^{-1}) is the specific heat of fresh ice at $0°$, $T_m(S)$ is the melting temperature of sea ice as determined by a salinity-dependent liquidus relation, L_0 ($= 334$ kJ kg^{-1}) is the latent heat of fusion of fresh ice at $0°$ and c_w is the specific heat capacity of brine.

3.1.3 Ice congelation

The amount of ice congelation or melt at the ice bottom is given by the imbalance between F_{bot} and the conductive heat flux adjacent to the ice base (F_{cb}), according to:

$$q(T,S)\frac{\partial h}{\partial t} = (F_{bot} - F_{cb}), \tag{6}$$

where q is the enthalpy at the ice bottom interface as given from Eq. 5. F_{cb} is defined as:

$$F_{cb} = K_b \frac{2(T_n - T_b)}{\Delta h_n}, \tag{7}$$

where K_b, T_b are the conductivity and temperature at the ice/ocean interface and T_n, Δh_n are the temperature and thickness of the lowest ice layer.

3.2 Snow-ice formation

The formation of snow-ice is represented by converting a fraction of the snow layer to sea ice whenever the hydrostatic balance pushes the snow-ice interface below the water line. This conversion is mass-conserving and instantaneous. The threshold for snow-ice formation is based on Archimedes' law:

$$h_s > \frac{(\rho_w - \rho_i)h_i}{\rho_s}, \tag{8}$$

where h_s is the snow thickness. The change in snow and ice thicknesses ($\delta h_s, \delta h_i$) associated with snow-ice formation is written as:

$$\delta h_s = \frac{-\rho_i h^*}{\rho_w},\tag{9}$$

$$\delta h_i = \frac{\rho_s h^*}{\rho_w},\tag{10}$$

where h^* is the amount of snow in excess of the hydrostatic equilibrium thickness before the snow-ice conversion.

3.3 Mushy layer thermodynamics

3.3.1 Enthalpy, temperature and salinity profiles

In the mushy layer thermodynamics, sea ice is assumed to be a mixed-phase layer composed of both fresh ice and liquid brine inclusions, with proportions that are determined by prognostic temperature and salinity relations (Feltham et al., 2006; Turner et al., 2013). The boundary conditions at the top and bottom interface are the same as in the BL99 parameterization but the internal temperatures in the snow and ice layers are governed by a prognostic equation for enthalpy:

$$\frac{\partial q}{\partial t} = \frac{\partial}{\partial z}\left(K_i \frac{\partial T_i}{\partial z}\right) + w\frac{\partial q_{br}}{\partial z} - \frac{\partial}{\partial z}\left(I_{pen}(z)\right),\tag{11}$$

where q_{br} is the enthalpy of the brine and w is the Darcy velocity of the brine. The enthalpy q is defined in terms of the brine fraction and temperature, as:

$$\begin{aligned} q &= \phi q_{br} + (1-\phi)q_i \\ &= \phi \rho_w c_w T + (1-\phi)(\rho_i c_i T - \rho_i L_0) \end{aligned}\tag{12}$$

where q_i is the enthalpy of fresh ice and ϕ is the liquid fraction defined as:

$$\phi = \frac{S}{S_{br}},\tag{13}$$

where S_{br} is the salinity of the brine as defined by an observation-based liquidus relation (Turner et al., 2013). Together, equations 11 and 12 differ from the BL99 thermodynamics only from the additional heat advection from brine flow and the mixed-phase enthalpy definition.

The prognostic salinity equation in each ice layer includes dependencies on brine processes such as gravity drainage and melt pond flushing (Notz and Worster, 2009; Turner et al., 2013). It is is written as (Turner et al., 2013):

$$\frac{\partial S}{\partial t} + v_z \frac{\partial S_{br}}{\partial z} = \left.\frac{\partial S}{\partial t}\right|_{slow},\tag{14}$$

where v_z is the vertical velocity of the ocean water percolating upward through the ice layer in response to the brine drainage (rapid drainage mode). The right hand side represents a slow mode of brine drainage that varies with the surface temperature,

according to:

$$\frac{\partial S}{\partial t}\bigg|_{slow} = \begin{cases} -\omega(S - \phi_c S_{br})\frac{(T_{bot}-T_{sf})}{h_i}, & \text{if } T_{bot} > T_{sf}, \\ 0 & \text{otherwise.} \end{cases} \tag{15}$$

where ω is a tuning parameter set by the user (-5.0×10^{-9} m s^{-1} is the default value) determining the strength of the slow drainage and ϕ_c is a critical liquid fraction for the slow drainage to occur, also set by the user (0.05 is the default value in Icepack). More details can be found in Turner et al. (2013).

3.3.2 Standard mushy layer congelation

In mushy layer physics, there is no sharp interface between solid ice and ocean water, but rather a downward transition within the mush medium towards a 100% liquid fraction. As such, ice congelation is not made by forming a layer of solid ice but by moving the ice-ocean boundary at a rate defined by the conductive heat flux imbalance, and then by integrating the corresponding amount of sea water in the bottom ice layer. The solidification of the sea water is thus only treated in subsequent timesteps when implicitly solving for the temperature profiles, during which the liquid fraction is adjusted to satisfy the liquidus relation.

Specifically, the congelation rate (i.e. the migration of the ice-ocean boundary) is first defined based on the energy needed to form a mush layer with a congelation initial liquid fraction ϕ_{init}=0.85 (default value):

$$\frac{\partial h}{\partial t} = \frac{F_{bot} - F_{cb}}{-L\rho_i(1 - \phi_{init})}. \tag{16}$$

Then, the enthalpy and salinity of the lowest ice layer are updated by integrating the freezing sea water spanned by the moving boundary, according to:

$$\frac{\partial q_N}{\partial t} = \frac{1}{h}\frac{\partial h}{\partial t}(q_N - q_w), \tag{17}$$

$$\frac{\partial S_N}{\partial t} = \frac{1}{h}\frac{\partial h}{\partial t}(S_N - S_c), \tag{18}$$

where the subscript N refers to the last ice layer, q_w is the enthalpy of sea water at the freezing point and S_c is the bulk salinity of the integrated sea water (i.e. SSS).

Note that in this scheme, the enthalpy of the incorporated sea water is not fully accounting for conductive heat imbalance. This leads to a leftover being sent to the ocean, resulting in either a cooling of the SST, or, if the SST is at the freezing point, to frazil formation. The basal ice growth in our mushy layer simulations is thus obtained by combining the congelation growth/melt and the frazil (see Appendix A for more details).

Given a remaining heat flux imbalance F_{ocn} at the ice-ocean interface after congelation, the rate of frazil formation is defined as:

$$\frac{\partial h_f}{\partial t} = \frac{F_{ocn}}{q_f}, \tag{19}$$

where q_f is the enthalpy of the frazil as defined from Eq. 12, using a liquid fraction of 0.75 (smaller than ϕ_{init} for congelation) and temperature corresponding to the liquidus for a brine salinity of $S_{br} = SSS - 3$ (see Appendix A for more details).

3.3.3 Modified mushy layer congelation

To improve our mushy simulation results, we propose a modification to the congelation parameterization that reduces the frazil formation. In this new scheme, the migration of the ice-ocean boundary is determined by the energy needed to decrease the enthalpy of the original sea water to that of the new congelation mush. We assume that the solid ice formation is simultaneous with the moving boundary, such that the congelation mush layer with liquid fraction ϕ_{init} is explicitly incorporated into the lowest ice layer (instead of the sea water in the standard parameterization described above). This ensures that the enthalpy of the added congelation layer corresponds with the conductive heat imbalance at the ice-ocean interface, with no leftover sent to the ocean. More details can be found in Appendix B.

Specifically, the mushy congelation rate (i.e. the migration of the ice-ocean boundary) is now defined as:

$$\frac{\partial h}{\partial t} = \frac{F_{bot} - F_{cb}}{q_m - q_w}, \tag{20}$$

where q_m is the enthalpy of the integrated congelation mush layer as defined by Eq. 12, with a liquid fraction ϕ_{init} and at freezing point temperature. The enthalpy and salinity of the lowest ice layer is updated by integrating the congelation mush layer spanned by the moving boundary:

$$\frac{\partial q_N}{\partial t} = \frac{1}{h}\frac{\partial h}{\partial t}(q_N - q_m), \tag{21}$$

$$\frac{\partial S_N}{\partial t} = \frac{1}{h}\frac{\partial h}{\partial t}(S_N - \phi_{init}S_{br}), \tag{22}$$

with $S_{br} =$SSS.

3.3.4 Snow-ice formation

In the mushy layer scheme, the snow-ice formation remains based on the hydrostatic balance (Eq. 8), but the conversion of snow to ice is no longer mass-conserving (in stand alone simulations). Instead, it is assumed that sea-water is advected laterally or percolates through the ice layer, and sea water is added to fill the porosity of the snow layer. The change in snow and ice thicknesses are given by:

$$\delta h_i = -\delta h_s = \frac{m_{fb}}{\rho_w - \rho_s + \rho_{snice}}, \tag{23}$$

where m_{fb} ($= h_i\rho_i + h_s\rho_s - h_i\rho_w$) is the combined mass of snow and ice in excess of the hydrostatic equilibrium prior to the snow-ice formation and ρ_{snice} is the density of the newly formed snow-ice. The snow-ice density and liquid fraction ϕ_{snice} are defined by assuming that sea-water has filled the porosity of the snow-layer:

$$\phi_{snice} = 1 - \rho_s/\rho_i, \tag{24}$$

$$\rho_{snice} = \rho_w \phi_{snice} + \rho_i (1 - \phi_{snice}). \tag{25}$$

In this analysis, we also test the inclusion of snow flooding criteria in the snow-ice parameterization. In these specific simulations, the flooding onset is either based on a liquid fraction criterion or specifically set to the observed flooding onset date (i.e., as in Duarte et al., 2020). To avoid a large and sudden snow flooding, we include a simple linear dependence of the flooding rate on the negative freeboard:

$$\delta h_i = -\delta h_s = \gamma \frac{m_{fb}}{\rho_w - \rho_s + \rho_{snice}}, \tag{26}$$

where γ is a free parameter set here to 0.01 to match the observations.

4 Methods

4.1 Snow depth and ice thickness retrieval

The in-situ snow depth, ice thickness, congelation growth and snow-ice formation are determined using a new automated surface retrieval algorithm. Our algorithm is similar to that of Liao et al. (2019); Cheng et al. (2020) with a few adaptations that aim to reduce its sensitivity to large diurnal cycles and to improve its performance in near-isothermal conditions. As in Cheng et al. (2020), it is built to detect snow flooding, which was suspected at our deployment sites, and detects the material interfaces based on the vertical gradients in the temperature profiles. Similar vertical-gradient-based algorithms were recently shown to be most appropriate compared to other methods for the automated retrieval of ice thickness from IMB data (Gough et al., 2012; Richter et al., 2023).

The ice thickness and snow depths are determined from the position of three material interfaces on the SIMBA temperature profiles: the top of the snow layer (the air-snow interface, Z_{a-s} in Fig. 2), the snow/ice interface (Z_{s-i}) and the bottom ice-ocean interface (Z_{i-o}). Since a segment of the thermistor string is laid flat (horizontal) on the ice surface at deployment, the algorithm also needs to identify the first (Z_{ice0} in Fig. 2) and last (Z_p) sensors of this "thermistor plateau", which becomes embedded in the ice after flooding events (see Fig. 2b for the flooded ice case). These locations are first detected for each individual profiles (at a 6h interval), then smoothed using a 24h running mean to remove any sensitivity to the diurnal cycles.

The ice thickness h_i (including snow-ice), snow depth h_s and snow-ice thickness h_{si} are calculated from the five identified positions, according to:

$$h_i = Z_p - Z_{i-o} + Z_{s-i} - Z_{ice0}, \tag{27}$$

$$h_s = Z_{a-s} - Z_{s-i}, \tag{28}$$

$$h_{si} = Z_{s-i} - Z_{ice0}. \tag{29}$$

The changes in ice thickness can thus be associated with a displacement of the snow-ice interface (defining the snow-ice contribution to the mass balance), or the ice bottom interface (defining the congelation contribution to the mass balance).

The surface retrieval algorithm is based on the following assumptions:

1. The temperature profiles are piece-wise linear.

2. The ice surface does not move downward along the thermistor string (i.e., no vertical slip between the buoys and the ice, and no surface melting).

3. The minimum temperature along the thermistor string is located above the snow layer.

4. The vertical profiles are isothermal in the atmosphere and in the ocean.

These assumptions are similar to those from Liao et al. (2019); Zuo et al. (2018); Cheng et al. (2020), and relate to the dependency of the algorithm on the difference in heat conductivity (i.e. vertical temperature gradient) in the snow and ice layers. Heat-conductivity based surface retrieval algorithms are thus, by construction, not suited for near isothermal conditions (e.g. during thaw), in which case other observations (e.g. from sonar data or the SIMBA heat cycles) are needed to determine the ice mass balance. The algorithm described below is similar in principle to that of Cheng et al. (2020) and only differs in the detection criteria for each interface.

4.1.1 Temperature gradient and curvature

The vertical temperature gradient β and curvature γ are first calculated at each sensor location and for the entire data record using a centered finite difference scheme. The vertical temperature gradient at the kth sensor location is defined as:

$$\beta_k = \frac{\partial T_k}{\partial z} \sim \frac{T_{k+1} - T_{k-1}}{2\Delta z}. \tag{30}$$

where T_k represent the temperature reading of the kth sensor and Δz is the spacing between two sensors (here 2 cm). The curvature at point k is defined as:

$$\gamma_k = \frac{\partial^2 T_k}{\partial z^2} \sim \frac{T_{k+1} - 2T_k + T_{k-1}}{\Delta z^2}, \tag{31}$$

4.1.2 Initial ice surface and thermistor plateau

For each buoy, the thermistor plateau is set at deployment and remains fixed over the entire record. The initial ice surface Z_{ice0} (with temperature T_{ice0}) and lower end of the thermistor plateau serve as reference points for the algorithm.

The position Z_{ice0} is identified by the minimum curvature ($\min(\gamma_k)$) below the maximum vertical temperature gradient in the profiles (assumed to be inside the snow layer, Fig. 2). The other end of the thermistor plateau Z_p is identified by the closest local maxima in curvature below Z_{ice0}. To remove sensitivity to sporadic variations in the detected interfaces ($\pm 2cm$), the reference locations are defined as the statistical mode of Z_{ice0} and Z_p over the first 7 days of records.

4.1.3 Ice-ocean interface

For each profile, the position of the ice-ocean interface is determined using a minimization approach to find the sensor location best matching the corresponding change in the vertical temperature slope. That is, to each tentative ice bottom position Z_l,

where l represents a specific sensor location $k = l$ close to the expected ice bottom, we assign a theoretical piece-wise linear vertical temperature profile, defined as:

$$T_k^{th} = \begin{cases} T_c + (z_k - Z_c)\beta_{ice} & \text{if } Z_c > z_k > Z_l \\ T_w & \text{if } z_k < Z_l \end{cases} \tag{32}$$

where T_k^{th} is the theoretical temperature at sensor location z_k, T_c is the temperature observed at a position Z_c in the ice interior (here defined as $T_c \sim T_w + r(T_{ice0} - T_w)$, where $r = 1/3$ is an arbitrary ratio), β_{ice} is an ice temperature gradient initial guess and T_w is the observed ocean temperature. The initial guess β_{ice} is defined as:

$$\beta_{ice} = \frac{T_w - T_c}{Z_b - Z_c}. \tag{33}$$

The position of the ice bottom interface Z_{i-o} is then defined from the position Z_l with the theoretical profile that minimizes the following error function:

$$err = \sum_{k=l-10}^{l+10} (T_k^{th} - T_k^{obs})^2, \tag{34}$$

where T_k^{obs} is the observed temperature at sensor position k.

Note that this detection method differs significantly from the temperature selection method of Liao et al. (2019) and Cheng et al. (2020), with the benefit of not depending on the sensor type and precision.

4.1.4 Air-snow interface

The air-snow interface position Z_{a-s} is found by identifying the maximum vertical temperature curvature γ_k below the sensor with the coldest temperature reading (assumed to be in the air) and above the initial ice surface Z_{ice0}. The temperature gradient directly below Z_{ice0} must also be smaller than a threshold for snow detection, set to 0.1 °C cm^{-1}. Note that this threshold is smaller than in Liao et al. (2019) but is only used to discriminate curvatures associated with noise in the data. The temperature gradient in the snow layer is then defined as:

$$\beta_{snow} = \frac{T_{ice0} - T_{a-s}}{Z_{ice0} - Z_{a-s}}, \tag{35}$$

where T_{a-s} is the temperature reading at Z_{a-s}.

4.1.5 Snow-ice interface

The presence of snow-ice above the initial ice surface is detected by comparing the temperature gradient directly above the initial ice surface Z_{ice0} with β_{snow} and β_{ice}. That is, sensors above the original ice surface are associated with snow-ice if the local temperature gradient satisfies:

$$\beta_k < \beta_{ice} + r_{si}(\beta_{snow} - \beta{ice}), \tag{36}$$

where r_{si} ($= 1/5$) is a ratio between 0 and 1. If such a gradient is present above Z_{ice0}, the new ice surface position (Z_{s-i}) is updated to the lowest point where $\beta_k < \beta_{si}$ but only if holding for at least 4 days.

Note that while arbitrary, the ratio r_{si} for snow-ice detection ensures that the snow-ice conductivity is closer to that of sea-ice, while filtering fluctuations due to changing temperature conditions. The snow-ice detection is the only component of the algorithm that depends on the other detected interfaces.

4.2 Freeboard computation

The ice freeboard h_{fb} is the elevation of the snow-ice interface above the water line. A negative freeboard value indicates that the snow-ice interface is below the water line, with the ice in hydrostatic imbalance. In both the observations and simulations, we compute the freeboard based on the hydrostatic balance and the material parameters as defined in Icepack (see section 3):

$$h_{fb} = h_i - \frac{\rho_s h_s + \rho_i h_i}{\rho_w}. \tag{37}$$

Based on the propagation of uncertainty and assuming an error of 2 cm for the snow/ice thicknesses and of 33 kg m^3 for the snow density (King et al., 2020), these freeboard estimates have a precision of $\sim$1.0 cm.

4.3 Experiment setup

Multiple Icepack simulations are run with the BL99 or the mushy layer physics to reproduce each of the SIMBA observations, using standard and modified parameterizations (see Tables 1 and 2 for the full list of simulations and parameter specifications). All simulations use 7 ice layers, 1 snow layer and are initialized using the ice thickness, snow depth and internal ice temperature (at the location corresponding to the center of the snow and 7 ice layers) recorded by the buoys. The initialisation values are taken on March 1st, a few days after the SIMBA deployment to ensure that the deployment holes are completely refrozen. The simulations are run with a time-step of one hour (outputs only every 3 hours) from March 1st until well past the buoy recovery date. Results are only shown for the period corresponding with observations.

4.4 Model evaluation

The performance of each simulations is quantified using the Mean Integrated Error (MIE) of the ice thickness, snow depth, cumulative congelation and snow-ice formation. For each variable, the MIE is calculated first by linearly interpolating the SIMBA and simulation data into a hourly time-series. The MIE is then defined as:

$$MIE = \sum_{\tau=1}^{n} \frac{(X_{sim}^{\tau} - X_{obs}^{\tau})}{n}, \tag{38}$$

where n is the number of valid data points in the time series and (X_{sim}^{τ}, X_{obs}^{τ}) are the simulated and observed variable values at time τ.

5   Results

5.1   In-situ landfast ice thermodynamics

5.1.1   Observed temperature and weather conditions

The late winter conditions along the Labrador coast are characterised by increasingly large diurnal cycles in air temperature, with longer (synoptic) time scale events of colder or warmer weather (Fig. 3a). The 2-m air temperatures calculated from the GDPS data correspond well with the air temperatures recorded in-situ, but is generally colder (MIE of -0.78°C -0.58°C compared to the IMB1 and IMB2 records respectively). These biases are mostly associated with differences in the short term temperature peaks, the buoys recording larger maxima in air temperatures than represented in the GDPS data.

Several precipitation events occurred during the observational periods. The snow precipitation events from the GDPS data correspond well with the precipitations recorded at a nearby weather station (Nain airport, Fig. 3b). The precipitation phases were not documented in the airport records, and all events were snowfalls in the GDPS data. In particular, two events with heavy snowfalls are recorded on March 9-11 and April 6-10, which also correspond to periods of warmer weather during which temperatures slightly exceeded the freezing point.

The vertical temperatures recorded along the two SIMBA thermistor strings are coherent with these patterns (Fig. 3c-d). Short-term variations in air temperature are rapidly damped in the snow layer although heat from longer periods of warm weather reach and have a larger impact on the ice interior. The downward propagation of the surface heat is often followed by a slower cooling once colder conditions return. Despite the similar air temperature patterns, the IMB2 SIMBA recorded significantly warmer ice temperatures than IMB1, with a sharp warming events (see purple arrow in Fig. 3d) that suggest a snow flooding onset (Provost et al., 2017).

5.1.2   Surface retrieval algorithm validation

The surface retrieval algorithm is able to identify the snow and ice interfaces in most of the records (Fig 3c-d). The algorithm fails during the two warm spells when negligible vertical temperature gradients or temperature inversions are present within the snow and ice layers (i.e. the piece-wise linear assumption does not hold). The surface retrieval algorithm is also generally not successful during the melt season (beyond April 16th) for the same reason, except on occasional colder days.

While we do not have independent data to validate the retrieved snow and ice thicknesses, we find that the selected interfaces are coherent with the interfaces detectable by visual inspection in the temperature profiles (Fig 3c-d). The detected snow interfaces correspond well with the layer within which most of the variability associated with diurnal cycles or synoptic systems are damped (Fig. 4a-b) and where large vertical temperature gradients are present (Fig. 4c-d). The algorithm detects an upward migration of the snow-ice interface (i.e. snow flooding, see the upward displacement of top black line, representing the snow-ice interface, above its original position) that also corresponds well with the warm temperatures recorded above the initial ice surface. In particular, the onset of flooding at the IMB2 site (on March 26th) coincides with a sudden warming event observed at the snow-ice interface, propagating upward in the snow layer despite a cooling in surface air temperature above (see profiles

at the purple arrow in Fig. 3d and 4b). This signal is expected when the snow flooding is caused by upward percolation or lateral advection of sea-water (Provost et al., 2017), since the warm sea water increases the snow-ice interface temperature and the heat later diffuses upward. In contrast, flooding by liquid precipitation or snow melting would show the entire snow layer at the freezing point. This could be the case at the IMB1 site, where flooding is only detected late in the observational record (on April 25th) when surface air temperatures above freezing are regularly present.

The top and bottom ice interfaces show good agreement with those seen in the recorded warming of sensors during the SIMBA heating cycles (Fig. 4e-f). The detected snow layers are also coherent with the thermistor string sections measuring the largest heating (smallest conductivity), although this is more difficult to assess with certainty due to the large variations within this layer, likely resulting from vertically varying snow density. Note that the IMB2 heat cycle records (Fig. 4f) present a rather smooth vertical gradient over 2-4 cm within the thermistor plateau, supposedly sitting on the snow/ice interface. We speculate that this is due to the thermistor plateau not being exactly horizontal on the ice surface, and suggests a ($\sim$1-2 cm) thickness uncertainty related to this deployment method for marking of the initial ice surface. This positional uncertainty remains for the entire record but is no-longer visible once the thermistor plateau is flooded.

5.1.3 In situ landfast ice mass balance

The SIMBA observations show large snow depths ($\sim$20-40 cm) over relatively thin ice ($\sim$75-100 cm) from the beginning of the records, and the measured freeboard occasionally dips to negative values (Fig. 5a). Both sites present significant snow depth increases during each warm events with a subsequent reduction likely resulting from snow compaction and redistribution by the winds. The snow depths are generally larger at the IMB2 site (by $\sim$ 5-10 cm), with a large but short-lived maxima of 50 cm likely resulting from snow accretion and subsequent removal by the winds around the buoy.

The local ice mass balance at the two sites is largely influenced by the snow layer thickness and its insulating effect on the sea ice below. The thinner snow cover at the IMB1 site results in colder internal ice temperatures, larger congelation rates at the ice base and less snow flooding (Fig. 5b). With an initial ice thickness and snow depth of 80 cm and 26 cm respectively (on March 1st), the IMB1 freeboard reach negative values after each snow fall event: -1.8 cm on March 13th and -1.6 cm on April 14th. Snow flooding is only detected from April 25th onward. The ice thickness reached its maximum (100 cm) on May 1st, for a total ice growth of 20 cm, from which 16 cm is associated with congelation at the ice-ocean interface and 4 cm is associated with snow-ice formation. In comparison, the IMB2 buoy initially recorded a 30 cm snow depth and 76 cm ice thickness (on March 1st), already corresponding to a negative freeboard (-1.6 cm). Snow falls during the first warm event brings the freeboard to a minimum of -6.4 cm on March 15th. Snow flooding is detected from March 25th onward, coinciding with a large ($\sim$10 cm) reduction in the snow depth. By April 6th, the ice thickness reached a maximum of 97 cm for a total ice growth of 21 cm, 13 cm of which is attributed to snow-ice formation and 8 cm to congelation.

5.2 BL99 simulations

The BL99 thermodynamics represents generally well the observed internal temperature profiles but with a larger downward heat conduction in the ice interior during periods of warm weather compared to the observations (Fig. 6). The simulated snow

thicknesses present large discrepancies with observations (MIE of +1.88 cm and -3.07 cm for IMB1 and IMB2, respectively),
mostly due to a lack of variation as the simple snow model does not account for snow compaction and redistribution. The
simulated ice thickness is in general accord with observations (Fig. 7a-b) with a small positive bias +0.25 cm (MIE) for IMB1
and +2.13 for IMB2 (see Tables 1 and 2). Despite the positive MIE values, the ice thickness at the time of the observed
maximum are smaller then the observed values, at 97.4 cm and 90.8 cm for the IMB1 and IMB2 simulations respectively
(-2.6 cm and -6.2 cm underestimations). Most of the ice growth is attributed to ice congelation at the ice bottom (14.9 cm and
10.5 cm), showing slowly decreasing ice growth rates from ~ 0.3 cm day^{-1} to near zero in May. The volume of snow ice is
largely underestimated at 2.4 and 4.3 cm (-1.6 cm and -8.7 cm underestimations), despite the fact that conditions for snow-ice
formation are met from the very start of the simulation (Fig. 7c-d).

The ice thickness and snow depth discrepancies are partly attributed to the misrepresentation of snow-ice formation, specifi-
cally to snow flooding onset being based only on the hydrostatic balance: the initialized snow depths being sufficient to depress
the ice surface near (or already below in the IMB2 case) the water line, any subsequent snow precipitation leads to a portion of
the snow cover being immediately transformed into snow-ice (Fig. 7a-b, orange lines for freeboard values and Fig. 7c-d, blue
lines for snow-ice volumes). This leads to the ice thickness temporarily exceeding the observations early in the simulations up
to the observed snow flooding unset, after which the thickness bias turns negative (in the IMB2 case) due to the small snow-ice
volume.

5.3 Mushy simulations

Compared to the BL99 simulations, the mushy layer physics produces warmer sea ice temperatures (see Fig. 6c-d) and faster
ice growth at both interfaces (i.e. snow-ice formation and bottom ice growth, see Fig. 8). These differences are present despite
the fact that the simulated snow depth are very similar in both simulations.

The ice thickness in the mushy simulations reached 103.8 cm and 97.5 cm for IMB1 and IMB2 respectively at the time
of the observed maximum, corresponding to 3.8 cm and 0.5 cm over-estimations. The ice growth presents larger variations
than observations due to a combination of spurious snow-ice formation and variable basal ice growth. The spurious snow-ice
formation is similar but larger than in the BL99 simulations, yielding large ice thickness discrepancies during the period with
observed negative freeboards. The total volume of snow ice is however closer to observations, with 8.0 cm and 13.0 cm for
the IMB1 and IMB2 simulations respectively (+4.0 cm and 0.0 cm deviations from observations). The basal growth variability
could be considered an asset when compared with the slowly-varying congelation rates in the BL99 simulations, but it is largely
over-estimated and effectively degrades the model performance. In particular, the simulated basal growth feature periods of
weak basal melt that are not coherent with observations (Fig. 8c-d). A quarter of the basal growth is attributed to the frazil
formation during periods of rapid congelation (see the Appendix, A). This frazil formation occurs despite the landfast ice
conditions, under 100% concentration sea ice with uniform thickness (1 category model), and is related to the treatment of the
ice-ocean boundary in the mushy congelation parameterization (see section 3.3.2 for details).

All simulations (BL99 and mushy) thus present discrepancies early in the simulations due to the hydrostatic balance criteria
not accounting for negative freeboards. This difficulty lead Duarte et al. (2020) to manually activate/deactivate the snow-ice

parameterization (i.e. by adding/removing the hydrostatic equilibrium condition according to the observations) to adequately reproduce in-situ conditions. In our experiment, deactivating the snow-ice parameterization in all simulations effectively allows the snow depth to increase during precipitation events (see thin lines in Fig. 7 and 8) and reduces the ice thickness discrepancy up to the flooding onset. This however leads to an underestimation of the ice thickness by the end of the simulations due to the missing snow-ice contribution in the ice mass balance. Note that the removal of snow-ice formation causes different responses in the BL99 and mushy layer thermodynamics. Using the BL99 physics, simulations without snow-ice show smaller congelation rates due to the increased insulation from the larger snow depths. Using the mushy layer physics, simulations without snow-ice show larger congelation rates despite the larger snow depths, since the ice interior is colder without the influx of warm ocean water associated with flooding, resulting in larger conductive heat fluxes at the ice base.

We note that while the mushy layer simulations quantitatively represent a degradation of the model performance (see larger MIE values in Tables 1 and 2), this is largely due to a snow flooding onset discrepancy combined with the wider ranging effects of the flooding on the ice thickness growth, interior ice salinity and temperatures. These effects, however, are physically meaningful and correspond well with previously recorded snow-flooding thermodynamics (see Provost et al., 2017, for instance). We find that adding a simple minimum porosity criterion ($\phi_{min} = 0.005$) to the snow-ice parameterization and setting the flooding rate inversely proportional to h_{fb} largely improves the IMB2 simulations by delaying the snow-ice formation by several days (Fig. 9b). The model in particular presents very small MIE values for snow-ice formation when the flooding onset is set manually to the observed date (Fig. 9c and Table 2).

5.4 Basal ice temperature, brine salinity and congelation

The inclusion of prognostic salinity and brine parameterizations in the mushy layer physics yields added model sensitivities relating to the liquidus relationship. That is, for a given salinity, the liquidus relation inter-connects changes in temperature with changes in brine salinity and liquid fraction. As such, updating the brine salinity in explicit parameterizations, such as the snow flooding or ice congelation parameterizations, later affects the layer temperature solved implicitly in subsequent time-steps. For instance, the sea water added in the upper ice layer in the snow-ice parameterization increases the layer bulk salinity but also dilutes the brine salinity towards SSS values. This effectively warms the layer according to the liquidus balance (Fig. 10). The layer temperature then slowly returns to colder values as the brine pockets refreeze, concentrating the brine salinity to its original value (see curves converging back to values from the negative freeboard simulations in Fig. 10a).

Similarly, the alternating periods of sea ice congelation and melt in the standard mushy layer simulations is attributed to a similar brine-temperature feedback in the lowest ice layer: any process reducing the brine salinity yields an increase in the layer temperature T_N. This reduces the conductive flux at the ice base (see Eq. 7, with T_f constant at the freezing point), and thus the available energy for congelation. Specifically, there are two explicit parameterizations inducing brine salinity changes at the ice base in the mushy layer thermodynamics: the brine drainage parameterizations (reducing the brine salinity), and the ice congelation (diluting the brine towards the SSS). These parameterizations act together in bringing the brine salinity close to SSS values early in the simulations (see blue curve Fig. 11c, for the ctrl simulation). Later brine drainage under cold weather further dilutes the brine to values below the SSS (and thus, $T_N > T_f$), causing a reversal of the conductive flux and sea ice

melt. This pattern can be suppressed by reducing the strength of the brine drainage (reducing the parameter ω, Fig. 11, left panels), although it also consequently yields too large congelation rates.

The basal ice growth can also be improved by modifying the congelation parameterization to reduce the associated salinity increase (Fig. 11, right panels). To do so, we repeat the experiments using a modified congelation scheme in which a mush layer with liquid fraction ϕ_{init} and S_{br} =SSS is incorporated in the lowest ice layer during congelation (see section 3.3.3 and Appendix B). Using this scheme, reducing the liquid fraction of congelation ice (ϕ_{init}) results in smaller congelation rates and salinity in the lowest ice layer. This in turn reduces the strength of the brine drainage (a lower salinity in Eq. 15), diminishing the variations in congelation while bringing the congelation rates closer to observations.

6 Discussion and conclusions

In this study, the thermodynamic growth of landfast ice in the vicinity of Nain (Labrador) is investigated from two Scottish Association for Marine Science (SAMS) Snow Ice Mass Balance Apparatus (SIMBA) buoys deployed in winter 2017. The observed thermodynamics are reproduced using Icepack v1.1.0, the column thermodynamics package of the Community Ice Code (CICE) version 6, with two different physical schemes: the Bitz and Lipscomb (1999) physics that represents the thermodynamics currently used in the Environment and Climate Change Canada (ECCC) ice-ocean forecasting systems, and the mushy layer thermodynamics (Feltham et al., 2006; Notz and Worster, 2009; Turner et al., 2013) that includes new physics available in CICE6. The performance of Icepack in reproducing the IMB observations is assessed with a particular attention to the improvements associated with the use of the mushy layer physics. The contributions of this paper include a new automated surface retrieval algorithm to infer the ice and snow thicknesses from the IMB temperature records, a modified mushy layer congelation scheme less conducive to frazil formation and modifications to the snow-flooding parameterization to allow for negative freeboards and slow snow flooding rates.

The in-situ observations presented in this analysis are in line with a number of negative freeboard measurements reported in recent years in the Arctic (Rösel et al., 2018; Provost et al., 2017; Duarte et al., 2020), which are likely to become more frequent as the sea ice thins and precipitation increases in the transition to a seasonal ice cover (Merkouriadi et al., 2020). It remains however that snow flooding is relatively infrequent: our in situ snow flooding observations were associated with anomalous 2017 snow conditions that have not yet re-occurred in subsequent (2018-2023) landfast ice observation campaigns. The frequency at which snow flooding contributes to the ice mass balance in landfast ice areas, in Nain but also more widely along the Canadian Arctic, remains to be determined. Note however that as snow-ice formation occurs more easily over thin ice (Granskog et al., 2017), it is likely contributing to the ice growth early in the season and in new leads. This could be better assessed with IMB buoys deployed in open water prior to the freeze-up. Such a deployment was attempted in 2022 in Nain, but buoy icing, floe drifting and wave battering prevented the measurement of a continuous time series during the freeze-up period.

The large discrepancies between the observed and simulated snow flooding onset in the analysis joins the results of Duarte et al. (2020) in demonstrating that the use of the hydrostatic balance alone is insufficient to define snow flooding and to capture

the more complex processes observed in-situ (Eicken et al., 1995; Maksym and Jeffries, 2000; Provost et al., 2017). Our results show that while this conclusion also applies to the BL99 parameterization, the snow flooding exerts a much wider-ranging thermodynamic response under the mushy layer physics as the flooding increases the temperature, salinity and liquid fraction in the upper ice layers. It better represents the observed thermodynamics and is an improvement compared to the BL99 physics, as indicated by the smaller MIE values when the flooding onset is corrected according to the observations (see Table 2). One advantage of the mushy layer physics is that it contains the necessary ingredients to improve the snow flooding parameterization with additional porosity conditions for the percolation of sea-water through the brine channels.

In our analysis, no porosity criterion was found to reproduce the observed snow flooding onset date. This could indicate the influence of nearby sea ice dynamics, although in our case, the deployed IMBs were located in a well sheltered landfast channel dozens of kilometers away from the landfast ice edge. Moreover, the slow rate of snow-ice formation corresponds well with percolation through the porous sea ice medium (i.e., as opposed to the sudden flooding expected when flood water is advected laterally from neighboring deformation sites Provost et al., 2017). One difficulty in reproducing the snow flooding onset with porosity criteria is that they do not account for a percolation associated with the larger-scale porosity (e.g. from thermal cracking) unrelated to the smaller scale mushy layer characteristics. At the km-scale of most dynamical sea ice models, the volume of snow-ice will likely not be uniform over a grid-cell area. This is made evident in our results by the different in-situ flooding onset recorded by our two neighboring SIMBAs. Most likely, the snow-ice volume will be spatially distributed according to the ability of the flood water to penetrate the snow layer, and ultimately depending on the ice topography (ice thickness distribution), local snow conditions and the ice heterogeneity (i.e. the presence and average distance between cracks). The snow-ice volume at this scale would thus likely be better represented by a subgrid parameterization relating the snow conversion to a spatial probability for water penetration.

Our results further demonstrate that the mushy layer physics leads to a much larger salinity and temperature variability at the ice bottom, with significant sensitivity to new free parameters (e.g., ω, ϕ_{init}). This highly impacts the simulated ice congelation rates and, using the default Icepack parameters, yields to a degradation of the model performance despite the improved representation of brine processes. This performance is however mostly associated with the treatment of the brine salinity in the explicit congelation parameterization producing too large congelation rates, erroneous melt and significant frazil formation. The frazil formation in particular is not expected in our sheltered landfast context, but its over-representation is coherent with previous studies reporting large frazil volumes in pan-Arctic or Antarctic simulations using the mushy layer thermodynamics (Turner and Hunke, 2015; Bailey et al., 2020; DuVivier et al., 2021).

The mushy layer thermodynamics can nonetheless outperform the BL99 simulations using a simple modification to the congelation paramerization with a tuning of the initial congelation liquid fraction. Note however that the modified congelation is not salt-conserving (i.e. similarly to the frazil formation) and should be treated accordingly in the context of coupled simulations. The best model performance was obtained when the mushy layer physics was used with the modified congelation parameterisation, a reduced initial congelation liquid fraction and a manual snow flooding onset (Fig. 12). We note however that this represents significant tuning towards our SIMBA observations, which are not representative of typical high-Arctic conditions. As such, this tuning exercise is not meant to determine specific parameter values to be used in Icepack. It nonethe-

605 less demonstrates the need to better constraint the mushy layer parameters, which could be made in future work with larger sets of in-situ observations including salinity measurements.

Finally, we note that the increased sensitivity to physical processes in the mushy layer thermodynamics are likely to positively affect the landfast ice dynamics. For instance, the larger congelation rates simulated under colder air conditions may allow for faster sea ice consolidation (increasing the effective ice strength) and ease the formation of ice arches in narrow passages. The
610 impact of snow flooding, precipitation and surface melt on the ice interior via brine dynamics is also likely to increase the preconditionning from large scale ice strength heterogeneity early in the thaw season, which also could affect the timing and variability of landfast ice break up. The mushy layer thermodynamics thus presents itself as a useful, if not necessary, step towards improving the coupling between the thermodynamics and dynamics sea ice model components.

Code and data availability. All codes and data (model and analysis) are available on Zenodo (https://zenodo.org/record/8326693), and the
615 Icepackv1.1.0 used to produce the simulations is available on github, branch Plante.et.al.2023, at : https://github.com/mathieuslplante/Icepack.git.

Appendix A: Mushy congelation parameterization and frazil formation

In Icepack, the mushy congelation parameterization is composed of two components: the downward migration of the ice-ocean boundary, based on the computed congelation rate, and the integration of mass (sea water and/or fresh ice) in the bottom sea ice layer. In mushy layer physics, the ice-ocean interface is defined by the position where the mush medium reaches 100% liquid
620 fraction. Accordingly, the standard congelation parameterization assumes that its downward migration precedes the freezing of sea water, such that sea water without fresh ice is being added in the mush medium. Later solidification in the bottom ice layer occurs in subsequent timesteps when solving for the internal temperature profiles, via the liquidus relation. This however implies that the enthalpy used to define the congelation rate (i.e., Eq. 16, based on initial congelation liquid fraction ϕ_{init}) differs from the energy actually being integrated in the sea ice by congelation.
625 Specifically, defining $E_A = F_{bot} - F_{cb}$ as the energy available for congelation (i.e. the conductive heat imbalance at the ice-ocean interface) and E_U as the energy used during congelation (from Eq. 17), the fraction r of the available energy used by the mushy layer congelation can be written as:

$$r = \frac{E_U}{E_A} = \frac{q_w \frac{\partial h_c}{\partial t}}{F_{bot} - F_{cb}}, \tag{A1}$$

where h_c is the congelation ice thickness and $q_w = c_w \rho_w T$ is the enthalpy of sea water at the freezing point. Using Eq. 16, this
630 reduces to:

$$\begin{aligned} r &= \frac{q_w}{-L_0 \rho_i (1 - \phi_{init})}, \\ &= -c_1 \frac{T}{1 - \phi_{init}} \end{aligned} \tag{A2}$$

where $c_1 = \rho_w c_w / L_0 \rho_i \sim 0.014$ and T is in Celsius. This demonstrate that unless ϕ_{init} is close to 1, we have $r < 1$ (e.g., using $\phi_{init} = 0.85$ and $T \sim -1.8°C$, we find r = 0.17) and the remaining energy imbalance is sent to the ocean. If there is no heat

transfer from below the mixed layer, this energy leads to frazil formation. Using Eq. 19 with $F_{ocn} = (1-r)U_A$, the ice growth from this frazil formation is given by:

$$\frac{\partial h_f}{\partial t} = \frac{1-r}{q_f} E_A. \tag{A3}$$

The total basal ice growth in the standard mushy layer physics is then obtained by adding Eq. 16 and A3:

$$\begin{aligned}
\frac{\partial h}{\partial t} &= \frac{\partial h_c}{\partial t} + \frac{\partial h_f}{\partial t} \\
&= \frac{r}{q_w} E_A + \frac{1-r}{q_f} E_A,
\end{aligned} \tag{A4}$$

where Eq. A2 has been used to rewrite the growth in terms of the available energy and the fraction r. This indicates that increasing the fraction r (e.g. by decreasing ϕ_{init}, see Eq. A2) decreases the congelation rate, also increases the amount of frazil formation by a proportional amount, resulting in similar total basal growth in the simulations (Fig 13).

Appendix B: Modified mushy congelation parameterization

Here, we propose a modified mushy congelation scheme that aims to reduce the amount of frazil formation. The modifications are two-fold: 1. the congelation rate is defined by the energy needed to bring sea water enthalpy to that of the integrated mushy and 2. the mass integrated in the lowest ice layer has a liquid fraction ϕ_{init}. This implies that some solidification occurs simultaneously as the ice-ocean interface migrates downward.

Specifically, instead of Eqs. 16, 17 and 18, we use:

$$\frac{\partial h_c}{\partial t} = \frac{F_{bot} - F_{cb}}{q_m - q_w}, \tag{B1}$$

$$\frac{\partial q_N}{\partial t} = \frac{1}{h} \frac{\partial h_c}{\partial t} (q_N - q_m), \tag{B2}$$

$$\frac{\partial S_N}{\partial t} = \frac{1}{h} \frac{\partial h_c}{\partial t} (S_N - \phi_{init} S_{br}), \tag{B3}$$

where q_m is the enthalpy of the integrated layer as defined by Eq. 12 with liquid fraction ϕ_{init} and temperature at the freezing point. The energy integrated in the bottom ice layer thus corresponds to:

$$E_U = q_m \frac{\partial h_c}{\partial t}, \tag{B4}$$

and the fraction r of the available energy used by the modified mushy layer congelation is:

$$\begin{aligned}
r &= \frac{q_w \frac{\partial h_c}{\partial t}}{F_{bot} - F_{cb}}, \\
&= \frac{q_m}{q_m - q_w}.
\end{aligned} \tag{B5}$$

Given that $q_m << q_w$, we have $r \sim 1$ and the volume of frazil associated with congelation is negligible.

Using $\phi_{init} = 0.85$, the modified congelation schemes produces total basal growth rates similar to the ones simulated by the standard parameterization, but all of the growth is attributed to the congelation as there is no frazil formation (Fig. 14). The sensitivity to the parameter ϕ_{init} is however increased (Fig. 15), as the changes in ice congelation rates are no longer balanced by changes in frazil formation. This allows for better tuning with the observations.

Note that in this analysis, we define S_{br} =SSS to satisfy the liquidus at the boundary where $T = T_f$. This implies some salt rejection associated with congelation, and it should be treated accordingly when coupling with an ocean model. To keep the congelation salt-conserving, the brine salinity of the integrated mush layer could be set to S_{br} =SSS/ϕ_{init}. Note, however, that this does not satisfy the liquidus at boundary and would thus affect the simulated temperature in the lowest ice layer.

Author contributions. MP implemented Icepack v1.1.0 as a column model and produced the simulations with assistance from JFL, FR and FD. ATivy and JA deployed the ice mass balance buoys. MP coded the surface retrieval algorithm with contributions from GS. MP and ATurner coded the modified congelation scheme. MP, JFL, BT, FR, FD and GS analysed and discussed the results. MP wrote the manuscript with edits from JFL, BT, FR, GS, ATivy, ATurner and FD.

Competing interests. The authors declare that they have no conflict of interest.

Acknowledgements. We thank the Nunatsiavut Research Center for assistance and support for the ice mass balance buoy deployment and retrieval. We also thank thank Elizabeth Hunke, David Bailey, David Clemens-Sewall and Andrew Roberts for useful discussions on the mushy layer sea ice congelation scheme.

References

Bailey, D. A., Holland, M. M., DuVivier, A. K., Hunke, E. C., and Turner, A. K.: Impact of a New Sea Ice Thermodynamic Formulation in the CESM2 Sea Ice Component, Journal of Advances in Modeling Earth Systems, 12, e2020MS002 154, https://doi.org/https://doi.org/10.1029/2020MS002154, e2020MS002154 2020MS002154, 2020.

Barber, D., Hanesiak, J., Chan, W., and Piwowar, J.: Sea-ice and meteorological conditions in Northern Baffin Bay and the North Water polynya between 1979 and 1996, Atmosphere-Ocean, 39, 343–359, https://doi.org/10.1080/07055900.2001.9649685, 2001.

Bitz, C. M. and Lipscomb, W. H.: An energy-conserving thermodynamic model of sea ice, Journal of Geophysical Research: Oceans, 104, 15 669–15 677, https://doi.org/10.1029/1999JC900100, 1999.

Buehner, M., Morneau, J., and Charette, C.: Four-dimensional ensemble–variational data assimilation for global deterministic weather prediction, Nonlinear Processes Geophys., 20, 669–682, 2013.

Buehner, M., McTaggart-Cowan, R., Beaulne, A., Charette, C., Garand, L., Heilliette, S., Lapalme, E., Laroche, S., Macpherson, S. R., Morneau, J., and Zadra, A.: Implementation of Deterministic Weather Forecasting Systems Based on Ensemble–Variational Data Assimilation at Environment Canada. Part I: The Global System, Monthly Weather Review, 143, 2532 – 2559, https://doi.org/10.1175/MWR-D-14-00354.1, 2015.

Caixin, W., Bin, C., Keguang, W., Sebastian, G., and Olga, P.: Modelling snow ice and superimposed ice on landfast sea ice in Kongsfjorden, Svalbard, Polar Research, 34, https://doi.org/10.3402/polar.v34.20828, 2015.

Carmack, E. C. and Macdonald, R.: Oceanography of the Canadian Shelf of the Beaufort Sea: A Setting for Marine Life, Arctic, 55, 29–45, 2002.

Cheng, Y., Cheng, B., Zheng, F., Vihma, T., Kontu, A., Yang, Q., and Liao, Z.: Air/snow, snow/ice and ice/water interfaces detection from high-resolution vertical temperature profiles measured by ice mass-balance buoys on an Arctic lake, Annals of Glaciology, 61, 309–319, https://doi.org/10.1017/aog.2020.51, 2020.

Collins, W. D., Bitz, C. M., Blackmon, M. L., Bonan, G. B., Bretherton, C. S., Carton, J. A., Chang, P., Doney, S. C., Hack, J. J., Henderson, T. B., Kiehl, J. T., Large, W. G., McKenna, D. S., Santer, B. D., and Smith, R. D.: The Community Climate System Model Version 3 (CCSM3), Journal of Climate, 19, 2122 – 2143, https://doi.org/10.1175/JCLI3761.1, 2006.

Cooley, S. W., Ryan, J. C., Smith, L. C., Horvat, C., Pearson, B., Dale, B., and Lynch, A. H.: Coldest Canadian Arctic communities face greatest reductions in shorefast sea ice, Nature Climate Change, 10, 533–538, https://doi.org/10.1038/s41558-020-0757-5, 2020.

Côté, J., Desmarais, J.-G., Gravel, S., Méthot, A., Patoine, A., Roch, M., and Staniforth, A.: The Operational CMC–MRB Global Environmental Multiscale (GEM) Model. Part II: Results, Monthly Weather Review, 126, 1397 – 1418, https://doi.org/https://doi.org/10.1175/1520-0493(1998)126<1397:TOCMGE>2.0.CO;2, 1998a.

Côté, J., Gravel, S., Méthot, A., Patoine, A., Roch, M., and Staniforth, A.: The Operational CMC–MRB Global Environmental Multiscale (GEM) Model. Part I: Design Considerations and Formulation, Monthly Weather Review, 126, 1373 – 1395, https://doi.org/https://doi.org/10.1175/1520-0493(1998)126<1373:TOCMGE>2.0.CO;2, 1998b.

Dammann, D. O., Eriksson, L. E. B., Mahoney, A. R., Eicken, H., and Meyer, F. J.: Mapping pan-Arctic landfast sea ice stability using Sentinel-1 interferometry, The Cryosphere, 13, 557–577, https://doi.org/10.5194/tc-13-557-2019, 2019.

Divine, D. V., Korsnes, R., and Makshtas, A. P.: Temporal and spatial variation of shore-fast ice in the Kara Sea, Continental Shelf Research, 24, 1717–1736, https://doi.org/https://doi.org/10.1016/j.csr.2004.05.010, 2004.

Duarte, P., Sundfjord, A., Meyer, A., Hudson, S. R., Spreen, G., and Smedsrud, L. H.: Warm Atlantic Water Explains Observed Sea Ice Melt Rates North of Svalbard, Journal of Geophysical Research: Oceans, 125, e2019JC015 662, https://doi.org/https://doi.org/10.1029/2019JC015662, e2019JC015662 2019JC015662, 2020.

Dumont, D., Gratton, Y., and Arbetter, T. E.: Modeling the Dynamics of the North Water Polynya Ice Bridge, Journal of Physical Oceanography, 39, 1448 – 1461, https://doi.org/10.1175/2008JPO3965.1, 2009.

Dumont, D., Gratton, Y., and Arbetter, T. E.: Modeling Wind-Driven Circulation and Landfast Ice-Edge Processes during Polynya Events in Northern Baffin Bay, Journal of Physical Oceanography, 40, 1356 – 1372, https://doi.org/10.1175/2010JPO4292.1, 2010.

Dupont, F., Dumont, D., Lemieux, J.-F., Dumas-Lefebvre, E., and Caya, A.: A probabilistic seabed–ice keel interaction model, The Cryosphere, 16, 1963–1977, https://doi.org/10.5194/tc-16-1963-2022, 2022.

DuVivier, A. K., Holland, M. M., Landrum, L., Singh, H. A., Bailey, D. A., and Maroon, E. A.: Impacts of Sea Ice Mushy Thermodynamics in the Antarctic on the Coupled Earth System, Geophysical Research Letters, 48, e2021GL094 287, https://doi.org/https://doi.org/10.1029/2021GL094287, e2021GL094287 2021GL094287, 2021.

Eicken, H., Fischer, H., and Lemke, P.: Effects of the snow cover on Antarctic sea ice and potential modulation of its response to climate change, Annals of Glaciology, 21, 369–376, https://doi.org/10.3189/S0260305500016086, 1995.

Eicken, H., Jones, J., Meyer, F., Mahoney, A., Druckenmiller, M. L., Rohith, M., and Kambhamettu, C.: Environmental Security in Arctic Ice-Covered Seas: From Strategy to Tactics of Hazard Identification and Emergency Response, Marine Technology Society Journal, 45, 37–48, https://doi.org/doi:10.4031/MTSJ.45.3.1, 2011.

Feltham, D. L., Untersteiner, N., Wettlaufer, J. S., and Worster, M. G.: Sea ice is a mushy layer, Geophysical Research Letters, 33, https://doi.org/https://doi.org/10.1029/2006GL026290, 2006.

Flocco, D., Feltham, D. L., and Turner, A. K.: Incorporation of a physically based melt pond scheme into the sea ice component of a climate model, Journal of Geophysical Research: Oceans, 115, https://doi.org/https://doi.org/10.1029/2009JC005568, 2010.

Galley, R. J., Else, B. G. T., Howell, S. E. L., Lukovich, J. V., and Barber, D. G.: Landfast Sea Ice Conditions in the Canadian Arctic : 1983 – 2009, Arctic, 65, 133–144, 2012.

Gearheard, S., Matumeak, W., Angutikjuaq, I., Maslanik, J., Huntington, H. P., Leavitt, J., Kagak, D. M., Tigullaraq, G., and Barry, R. G.: "It's Not that Simple": A Collaborative Comparison of Sea Ice Environments, Their Uses, Observed Changes, and Adaptations in Barrow, Alaska, USA, and Clyde River, Nunavut, Canada, AMBIO: A Journal of the Human Environment, 35, 203 – 211, https://doi.org/10.1579/0044-7447(2006)35[203:INTSAC]2.0.CO;2, 2006.

Gough, A. J., Mahoney, A. R., Langhorne, P. J., Williams, M. J., Robinson, N. J., and Haskell, T. G.: Signatures of supercooling: McMurdo Sound platelet ice, Journal of Glaciology, 58, 38–50, https://doi.org/10.3189/2012JoG10J218, 2012.

Granskog, M. A., Rösel, A., Dodd, P. A., Divine, D., Gerland, S., Martma, T., and Leng, M. J.: Snow contribution to first-year and second-year Arctic sea ice mass balance north of Svalbard, Journal of Geophysical Research: Oceans, 122, 2539–2549, https://doi.org/https://doi.org/10.1002/2016JC012398, 2017.

Gultepe, I., Isaac, G. A., Williams, A., Marcotte, D., and Strawbridge, K. B.: Turbulent heat fluxes over leads and polynyas, and their effects on arctic clouds during FIRE.ACE: Aircraft observations for April 1998, Atmosphere-Ocean, 41, 15–34, https://doi.org/10.3137/ao.410102, 2003.

Hibler, W. D.: A dynamic thermodynamic sea ice model, Journal of Physical Oceanography, 9, 815–846, 1979.

Holland, M. M., Bailey, D. A., Briegleb, B. P., Light, B., and Hunke, E.: Improved Sea Ice Shortwave Radiation Physics in CCSM4: The Impact of Melt Ponds and Aerosols on Arctic Sea Ice, Journal of Climate, 25, 1413 – 1430, https://doi.org/10.1175/JCLI-D-11-00078.1, 2012.

750 Howell, S. E. L., Wohlleben, T., Dabboor, M., Derksen, C., Komarov, A., and Pizzolato, L.: Recent changes in the exchange of sea ice between the Arctic Ocean and the Canadian Arctic Archipelago, Journal of Geophysical Research: Oceans, 118, 3595–3607, https://doi.org/https://doi.org/10.1002/jgrc.20265, 2013.

Hunke, E. C. and Dukowicz, J. K.: An Elastic–Viscous–Plastic Model for Sea Ice Dynamics, Journal of Physical Oceanography, 27, 1849 – 1867, https://doi.org/10.1175/1520-0485(1997)027<1849:AEVPMF>2.0.CO;2, 1997.

755 Hunke, E. C., Lipscomb, W. H., Turner, A. K., Jeffery, N., and Elliott, S.: Cice: the los alamos sea ice model documentation and software user's manual version 4.1 la-cc-06-012, T-3 Fluid Dynamics Group, Los Alamos National Laboratory, 675, 500, 2010.

Hunke, E. C., Hebert, D. A., and Lecomte, O.: Level-ice melt ponds in the Los Alamos sea ice model, CICE, Ocean Modelling, 71, 26–42, https://doi.org/https://doi.org/10.1016/j.ocemod.2012.11.008, arctic Ocean, 2013.

Huwald, H., Tremblay, L.-B., and Blatter, H.: A multilayer sigma-coordinate thermodynamic sea ice model: Validation against Surface Heat

760 Budget of the Arctic Ocean (SHEBA)/Sea Ice Model Intercomparison Project Part 2 (SIMIP2) data, Journal of Geophysical Research: Oceans, 110, https://doi.org/https://doi.org/10.1029/2004JC002328, 2005.

Jackson, K., Wilkinson, J., Maksym, T., Meldrum, D., Beckers, J., Haas, C., and Mackenzie, D.: A Novel and Low-Cost Sea Ice Mass Balance Buoy, Journal of Atmospheric and Oceanic Technology, 30, 2676 – 2688, https://doi.org/10.1175/JTECH-D-13-00058.1, 2013.

King, J., Howell, S., Brady, M., Toose, P., Derksen, C., Haas, C., and Beckers, J.: Local-scale variability of snow density on Arctic sea ice,

765 The Cryosphere, 14, 4323–4339, https://doi.org/10.5194/tc-14-4323-2020, 2020.

Kirillov, S., Babb, D. G., Komarov, A. S., Dmitrenko, I., Ehn, J. K., Worden, E., Candlish, L., Rysgaard, S., and Barber, D. G.: On the Physical Settings of Ice Bridge Formation in Nares Strait, Journal of Geophysical Research: Oceans, 126, e2021JC017 331, https://doi.org/https://doi.org/10.1029/2021JC017331, e2021JC017331 2021JC017331, 2021.

Kwok, R.: Exchange of sea ice between the Arctic Ocean and the Canadian Arctic Archipelago, Geophysical Research Letters, 33, L16 501,

770 https://doi.org/https://doi.org/10.1029/2006GL027094, 2006.

Lemieux, J.-F., Tremblay, L. B., Dupont, F., Plante, M., Smith, G. C., and Dumont, D.: A basal stress parameterization for modeling landfast ice, Journal of Geophysical Research: Oceans, 120, 3157–3173, https://doi.org/https://doi.org/10.1002/2014JC010678, 2015.

Lemieux, J.-F., Dupont, F., Blain, P., Roy, F., Smith, G. C., and Flato, G. M.: Improving the simulation of landfast ice by combining tensile strength and a parameterization for grounded ridges, Journal of Geophysical Research: Oceans, 121, 7354–7368,

775 https://doi.org/https://doi.org/10.1002/2016JC012006, 2016.

Liao, Z., Cheng, B., Zhao, J., Vihma, T., Jackson, K., Yang, Q., Yang, Y., Zhang, L., Li, Z., Qiu, Y., and Cheng, X.: Snow depth and ice thickness derived from SIMBA ice mass balance buoy data using an automated algorithm, International Journal of Digital Earth, 12, 962–979, https://doi.org/10.1080/17538947.2018.1545877, 2019.

Liu, Y., Losch, M., Hutter, N., and Mu, L.: A New Parameterization of Coastal Drag to Simulate Landfast Ice in Deep Marginal Seas

780 in the Arctic, Journal of Geophysical Research: Oceans, 127, e2022JC018 413, https://doi.org/https://doi.org/10.1029/2022JC018413, e2022JC018413 2022JC018413, 2022.

Lüpkes, C., Vihma, T., Birnbaum, G., and Wacker, U.: Influence of leads in sea ice on the temperature of the atmospheric boundary layer during polar night, Geophysical Research Letters, 35, L03 805, https://doi.org/10.1029/2007GL032461, 2008.

Madec, G. and the NEMO team: NEMO ocean engine, Note du Pole de modélisation 27, Institut Pierre-Simon Laplace (IPSL), France, 2008.

785 Madec, G., Delecluse, P., Imbard, M., and Levy, C.: OPA 8 Ocean General Circulation Model - Reference Manual, Tech. rep., LODYC/IPSL Note 11, 1998.

Maksym, T. and Jeffries, M. O.: A one-dimensional percolation model of flooding and snow ice formation on Antarctic sea ice, Journal of Geophysical Research: Oceans, 105, 26 313–26 331, https://doi.org/https://doi.org/10.1029/2000JC900130, 2000.

Maykut, G. A. and Untersteiner, N.: Some results from a time-dependent thermodynamic model of sea ice, Journal of Geophysical Research

790 (1896-1977), 76, 1550–1575, https://doi.org/https://doi.org/10.1029/JC076i006p01550, 1971.

Melling, H.: Sea ice of the northern Canadian Arctic Archipelago, Journal of Geophysical Research: Oceans, 107, 2–1–2–21, https://doi.org/https://doi.org/10.1029/2001JC001102, 2002.

Melling, H., Gratton, Y., and Ingram, G.: Ocean circulation within the North Water polynya of Baffin Bay, Atmosphere-Ocean, 39, 301–325, https://doi.org/10.1080/07055900.2001.9649683, 2001.

795 Merkouriadi, I., Liston, G. E., Graham, R. M., and Granskog, M. A.: Quantifying the Potential for Snow-Ice Formation in the Arctic Ocean, Geophysical Research Letters, 47, e2019GL085 020, https://doi.org/https://doi.org/10.1029/2019GL085020, e2019GL085020 2019GL085020, 2020.

Notz, D. and Worster, M. G.: Desalination processes of sea ice revisited, Journal of Geophysical Research: Oceans, 114, https://doi.org/https://doi.org/10.1029/2008JC004885, 2009.

800 Planck, C. J., Whitlock, J., Polashenski, C., and Perovich, D.: The evolution of the seasonal ice mass balance buoy, Cold Regions Science and Technology, 165, 102 792, https://doi.org/https://doi.org/10.1016/j.coldregions.2019.102792, 2019.

Plante, M., Tremblay, B., Losch, M., and Lemieux, J.-F.: Landfast sea ice material properties derived from ice bridge simulations using the Maxwell elasto-brittle rheology, The Cryosphere, 14, 2137–2157, https://doi.org/10.5194/tc-14-2137-2020, 2020.

Pringle, D. J., Eicken, H., Trodahl, H. J., and Backstrom, L. G. E.: Thermal conductivity of landfast Antarctic and Arctic sea ice, Journal of

805 Geophysical Research: Oceans, 112, https://doi.org/https://doi.org/10.1029/2006JC003641, 2007.

Provost, C., Sennéchael, N., Miguet, J., Itkin, P., Rösel, A., Koenig, Z., Villacieros-Robineau, N., and Granskog, M. A.: Observations of flooding and snow-ice formation in a thinner Arctic sea-ice regime during the N-ICE2015 campaign: Influence of basal ice melt and storms, Journal of Geophysical Research: Oceans, 122, 7115–7134, https://doi.org/https://doi.org/10.1002/2016JC012011, 2017.

Raddatz, R. L., Asplin, M. G., Candlish, L., and Barber, D. G.: General Characteristics of the Atmospheric Boundary Layer Over a Flaw

810 Lead Polynya Region in Winter and Spring, Boundary-Layer Meteorology, 138, 321–335, https://doi.org/10.1007/s10546-010-9557-1, 2011.

Rampal, P., Bouillon, S., Ólason, E., and Morlighem, M.: neXtSIM: a new Lagrangian sea ice model, The Cryosphere, 10, 1055–1073, https://doi.org/10.5194/tc-10-1055-2016, 2016.

Richter, M. E., Leonard, G. H., Smith, I. J., Langhorne, P. J., Mahoney, A. R., and Parry, M.: Accuracy and precision when deriving sea-ice

815 thickness from thermistor strings: a comparison of methods, Journal of Glaciology, 69, 879–898, https://doi.org/10.1017/jog.2022.108, 2023.

Richter-Menge, J. A., Perovich, D. K., Elder, B. C., Claffey, K., Rigor, I., and Ortmeyer, M.: Ice mass-balance buoys: a tool for measuring and attributing changes in the thickness of the Arctic sea-ice cover, Annals of Glaciology, 44, 205–210, https://doi.org/10.3189/172756406781811727, 2006.

820 Rösel, A., Itkin, P., King, J., Divine, D., Wang, C., Granskog, M. A., Krumpen, T., and Gerland, S.: Thin Sea Ice, Thick Snow, and Widespread Negative Freeboard Observed During N-ICE2015 North of Svalbard, Journal of Geophysical Research: Oceans, 123, 1156–1176, https://doi.org/https://doi.org/10.1002/2017JC012865, 2018.

Semtner, A. J.: A Model for the Thermodynamic Growth of Sea Ice in Numerical Investigations of Climate, Journal of Physical Oceanography, 6, 379 – 389, https://doi.org/10.1175/1520-0485(1976)006<0379:AMFTTG>2.0.CO;2, 1976.

825 Smith, G. C., Roy, F., Mann, P., Dupont, F., Brasnett, B., Lemieux, J.-F., Laroche, S., and Bélair, S.: A new atmospheric dataset for forcing ice–ocean models: Evaluation of reforecasts using the Canadian global deterministic prediction system, Quarterly Journal of the Royal Meteorological Society, 140, 881–894, https://doi.org/https://doi.org/10.1002/qj.2194, 2014.

Smith, G. C., Bélanger, J.-M., Roy, F., Pellerin, P., Ritchie, H., Onu, K., Roch, M., Zadra, A., Colan, D. S., Winter, B., Fontecilla, J.-S., and Deacu, D.: Impact of Coupling with an Ice–Ocean Model on Global Medium-Range NWP Forecast Skill, Monthly Weather Review, 146,

830 1157 – 1180, https://doi.org/10.1175/MWR-D-17-0157.1, 2018.

Smith, G. C., Liu, Y., Benkiran, M., Chikhar, K., Surcel Colan, D., Gauthier, A.-A., Testut, C.-E., Dupont, F., Lei, J., Roy, F., Lemieux, J.-F., and Davidson, F.: The Regional Ice Ocean Prediction System v2: a pan-Canadian ocean analysis system using an online tidal harmonic analysis, Geoscientific Model Development, 14, 1445–1467, https://doi.org/10.5194/gmd-14-1445-2021, 2021.

Stirling, I.: The Biological Importance of Polynyas in the Canadian Arctic, Arctic, 33, 303–315, 1980.

835 Stirling, I.: The importance of polynyas, ice edges, and leads to marine mammals and birds, Journal of Marine Systems, 10, 9–21, https://doi.org/https://doi.org/10.1016/S0924-7963(96)00054-1, 1997.

Tian, Z., Cheng, B., Zhao, J., Vihma, T., Zhang, W., Li, Z., and Zhang, Z.: Observed and modelled snow and ice thickness in the Arctic Ocean with CHINARE buoy data, Acta Oceanologica Sinica, 36, 66–75, https://doi.org/10.1007/s13131-017-1020-4, 2017.

Tremblay, J.-E., Gratton, Y., Carmack, E. C., Payne, C. D., and Price, N. M.: Impact of the large-scale Arctic circulation and

840 the North Water Polynya on nutrient inventories in Baffin Bay, Journal of Geophysical Research: Oceans, 107, 26–1–26–14, https://doi.org/https://doi.org/10.1029/2000JC000595, 2002.

Tremblay, L.-B. and Mysak, L. A.: Modeling Sea Ice as a Granular Material, Including the Dilatancy Effect, Journal of Physical Oceanography, 27, 2342 – 2360, https://doi.org/10.1175/1520-0485(1997)027<2342:MSIAAG>2.0.CO;2, 1997.

Trodahl, H. J., McGuinness, M. J., Langhorne, P. J., Collins, K., Pantoja, A. E., Smith, I. J., and Haskell, T. G.:

845 Heat transport in McMurdo Sound first-year fast ice, Journal of Geophysical Research: Oceans, 105, 11 347–11 358, https://doi.org/https://doi.org/10.1029/1999JC000003, 2000.

Turner, A. K. and Hunke, E. C.: Impacts of a mushy-layer thermodynamic approach in global sea-ice simulations using the CICE sea-ice model, Journal of Geophysical Research: Oceans, 120, 1253–1275, https://doi.org/https://doi.org/10.1002/2014JC010358, 2015.

Turner, A. K., Hunke, E. C., and Bitz, C. M.: Two modes of sea-ice gravity drainage: A parameterization for large-scale modeling, Journal

850 of Geophysical Research: Oceans, 118, 2279–2294, https://doi.org/https://doi.org/10.1002/jgrc.20171, 2013.

Ungermann, M., Tremblay, L. B., Martin, T., and Losch, M.: Impact of the ice strength formulation on the performance of a sea ice thickness distribution model in the Arctic, Journal of Geophysical Research: Oceans, 122, 2090–2107, https://doi.org/https://doi.org/10.1002/2016JC012128, 2017.

West, A., Collins, M., and Blockley, E.: Using Arctic ice mass balance buoys for evaluation of modelled ice energy fluxes, Geoscientific

855 Model Development, 13, 4845–4868, https://doi.org/10.5194/gmd-13-4845-2020, 2020.

Wilchinsky, A. V. and Feltham, D. L.: A continuum anisotropic model of sea-ice dynamics, Proceedings of the Royal Society of London. Series A: Mathematical, Physical and Engineering Sciences, 460, 2105–2140, https://doi.org/10.1098/rspa.2004.1282, 2004.

Wongpan, P., Hughes, K. G., Langhorne, P. J., and Smith, I. J.: Brine Convection, Temperature Fluctuations, and Permeability in Winter Antarctic Land-Fast Sea Ice, Journal of Geophysical Research: Oceans, 123, 216–230,

860 https://doi.org/https://doi.org/10.1002/2017JC012999, 2018.

Zuo, G., Dou, Y., and Lei, R.: Discrimination Algorithm and Procedure of Snow Depth and Sea Ice Thickness Determination Using Measurements of the Vertical Ice Temperature Profile by the Ice-Tethered Buoys, Sensors, 18, https://doi.org/10.3390/s18124162, 2018.

Table 1. Parameters and performance (MIE), for all IMB1 simulations

Exp. name	Physics	Flood onset	Congelation	ϕ_{init}	w_b	MIE			
						h_i	h_s	h_{cgl}	h_{si}
Ctrl	BL99	hydrostatic	BL99	–	–	+0.25 cm	+1.88 cm	-0.82 cm	+0.86 cm
	BL99	no flooding	BL99	–	–	-1.29 cm	+5.40 cm	-1.09 cm	-0.50 cm
	Mushy	hydrostatic	standard	0.85	-5.0e-9	+6.44 cm	+0.87 cm	+2.14 cm	+4.27 cm
	Mushy	no flooding	standard	0.85	-5.0e-9	+2.73 cm	+5.39 cm	+2.92 cm	-0.50 cm
Flooding onset	BL99	Manual	BL99	–	–	-1.17 cm	+5.08 cm	-1.09 cm	-0.28 cm
	Mushy	$\phi_{min} = 0.005$	standard	0.85	-5.0e-9	+5.79 cm	+1.74 cm	+2.35 cm	+3.36 cm
	Mushy	$\phi_{min} = 0.006$	standard	0.85	-5.0e-9	+5.79 cm	+1.74 cm	+2.35 cm	+3.36 cm
	Mushy	$\phi_{min} = 0.007$	standard	0.85	-5.0e-9	+4.03 cm	+3.88 cm	+2.75 cm	+1.34 cm
	Mushy	Manual	standard	0.85	-5.0e-9	+3.11 cm	+4.98 cm	+2.92 cm	+0.26 cm
Brine physics	Mushy	no flooding	standard	0.85	-5.0e-9	+2.73 cm	+5.39 cm	+2.92 cm	-0.50 cm
	Mushy	no flooding	standard	0.85	-2.0e-9	+7.06 cm	+5.41 cm	+7.26 cm	-0.50 cm
	Mushy	no flooding	standard	0.85	-1.0e-9	+11.42 cm	+5.42 cm	+11.62 cm	-0.50 cm
	Mushy	no flooding	modified	0.85	-5.0e-9	+2.09 cm	+5.39 cm	+2.28 cm	-0.50 cm
	Mushy	no flooding	modified	0.65	-5.0e-9	+0.74 cm	+5.40 cm	+0.94 cm	-0.50 cm
	Mushy	no flooding	modified	0.45	-5.0e-9	-0.19 cm	+5.40 cm	-0.00 cm	-0.50 cm
Tuned	Mushy	Manual	modified	0.45	-5.0e-9	+0.18 cm	+4.99 cm	+0.02 cm	+0.25 cm

Table 2. Parameters and performance (MIE), for all IMB2 simulations

Exp. name	Physics	Flood onset	Congelation	ϕ_{init}	w_b	MIE			
						h_i	h_s	h_{cgl}	h_{si}
Ctrl	BL99	hydrostatic	BL99	–	–	+2.13 cm	-3.07 cm	+1.35 cm	+0.06 cm
	BL99	no flooding	BL99	–	–	-2.06 cm	+7.09 cm	+0.69 cm	-3.61 cm
	Mushy	hydrostatic	standard	0.85	-5.0e-9	+8.56 cm	-4.14 cm	+0.50 cm	+7.60 cm
	Mushy	no flooding	standard	0.85	-5.0e-9	+0.72 cm	+7.08 cm	+3.47 cm	-3.61 cm
Flooding onset	BL99	Manual	BL99	–	–	-1.06 cm	+3.62 cm	+0.72 cm	-2.33 cm
	Mushy	$\phi_{min} = 0.005$	standard	0.85	-5.0e-9	+7.23 cm	-1.77 cm	+1.63 cm	+5.23 cm
	Mushy	$\phi_{min} = 0.006$	standard	0.85	-5.0e-9	+7.23 cm	-1.77 cm	+1.63 cm	+5.23 cm
	Mushy	$\phi_{min} = 0.007$	standard	0.85	-5.0e-9	+0.72 cm	+6.11 cm	+3.47 cm	-2.72 cm
	Mushy	Manual	standard	0.85	-5.0e-9	+3.02 cm	+3.33 cm	+2.85 cm	+0.20 cm
Brine physics	Mushy	no flooding	standard	0.85	-5.0e-9	+0.72 cm	+7.08 cm	+3.47 cm	-3.61 cm
	Mushy	no flooding	standard	0.85	-2.0e-9	+2.26 cm	+7.09 cm	+5.01 cm	-3.61 cm
	Mushy	no flooding	standard	0.85	-1.0e-9	+7.16 cm	+7.09 cm	+9.91 cm	-3.61 cm
	Mushy	no flooding	modified	0.85	-5.0e-9	+0.17 cm	+7.08 cm	+2.92 cm	-3.61 cm
	Mushy	no flooding	modified	0.65	-5.0e-9	-0.84 cm	+7.09 cm	+1.91 cm	-3.61 cm
	Mushy	no flooding	modified	0.45	-5.0e-9	-1.50 cm	+7.09 cm	+1.25 cm	-3.61 cm
Tuned	Mushy	Manual	modified	0.45	-5.0e-9	+1.18 cm	+3.35 cm	+1.02 cm	+0.18 cm
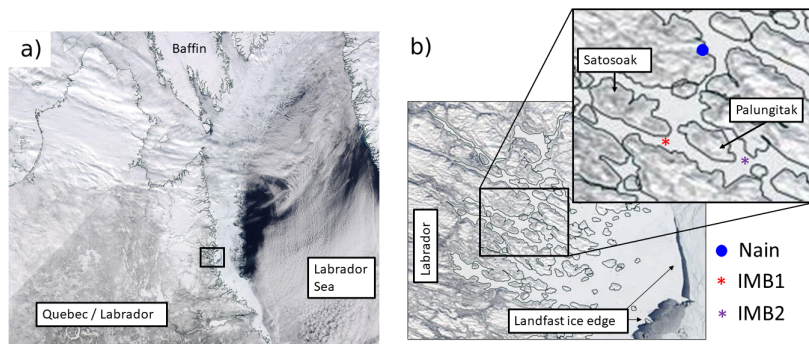
Figure 1. Location of the two IMB buoys on the Labrador coast (a), in a landfast ice channel close to the Nain community (b). The buoys are located at ∼56.42° N, 61.7° W (IMB1) and ∼56.43° N, 61.50°W,∼ (IMB2), 12 km from each other and ∼50 km from the nearest landfast ice edge. Images are corrected reflectance imagery taken from MODIS worldview (https://earthdata.nasa.gov/labs/worldview/).
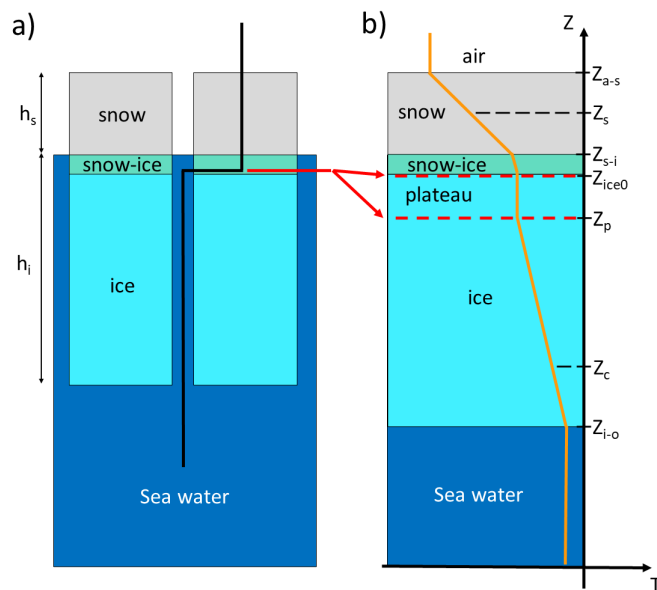
Figure 2. Schematics of the deployed SAMS IMB buoy thermistor strings through the snow, snow-ice and sea ice layers (a) and the vertical temperature profiles they measure (b) with the sensor positions used in the surface retrieval algorithm. Note the section of the thermistor string (thermistor plateau, red lines) laid flat on the bare ice surface at deployment but later embedded within the ice layer after flooding.
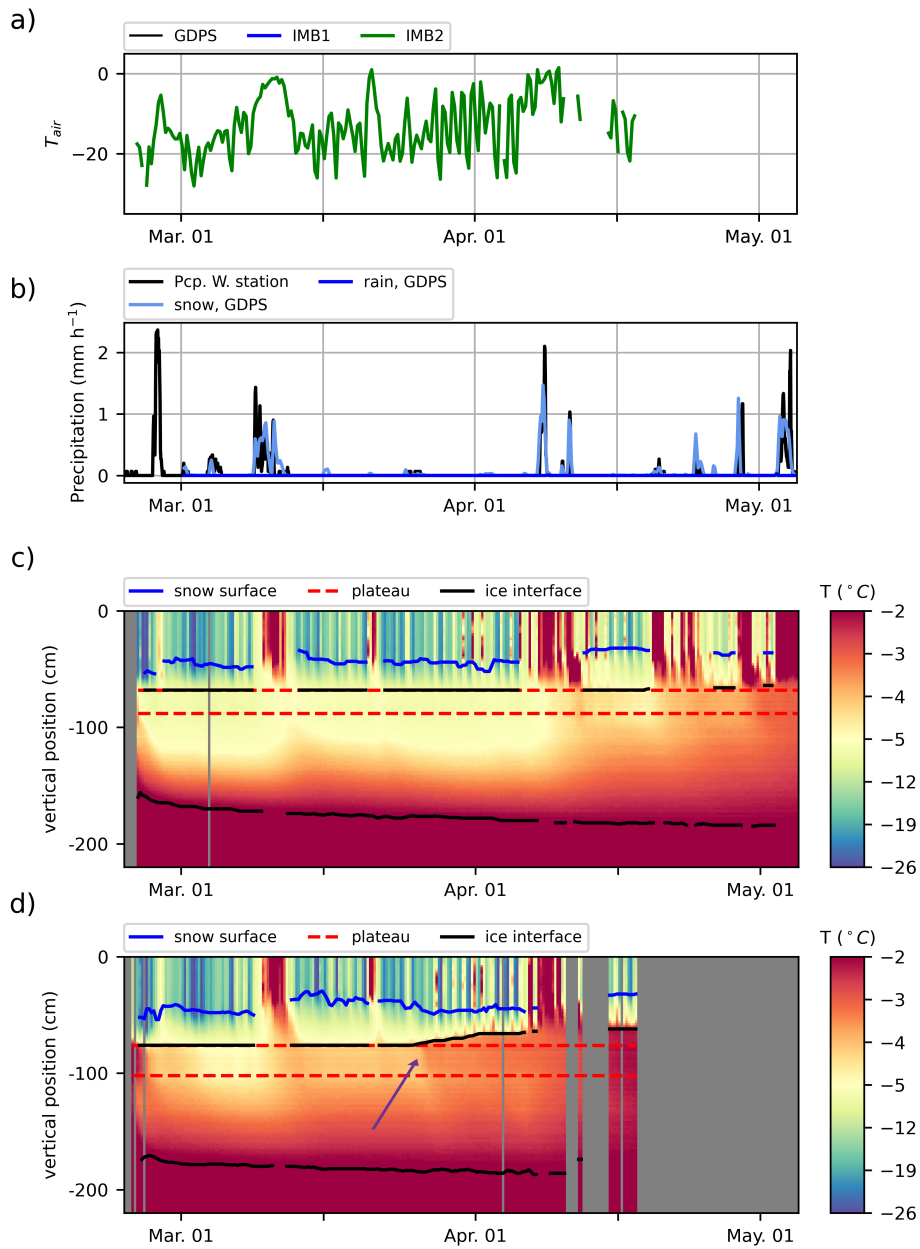
Figure 3. Time series of a) air temperature from the GDPS (black) and recorded by the IMB buoys (IMB1 in blue, IMB2 in green); b) precipitations from the Nain ECCC weather station (black) and from the GDPS (blue); c) recorded temperatures along the IMB1 thermistor string (color) with the detected material interfaces (air-snow interface in blue, ice surface and bottom in black and thermistor string plateau in red); d) Same as (c) but for the IMB2 buoy. The purple arrow points to the warming at the snow/ice interface, indicating flooding.
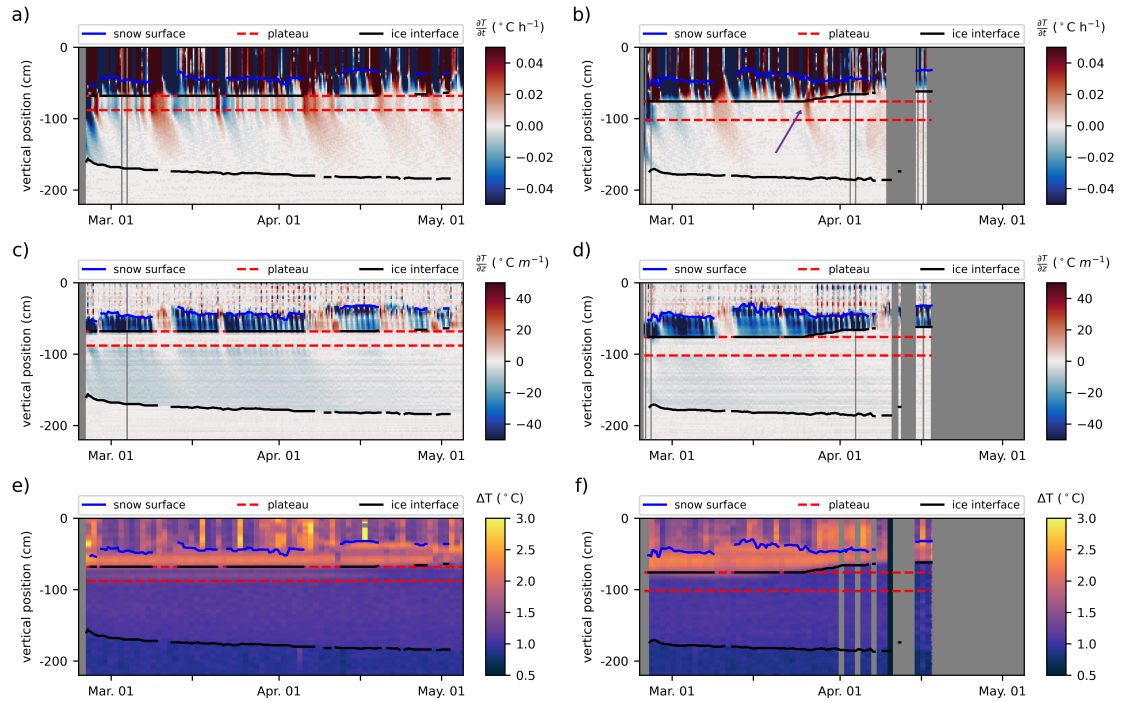
Figure 4. Rates of temperature changes (a, b, in color), vertical temperature gradients (c,d, in color) and change in temperature recorded after 2 min of heating during the daily heating cycles (e, f, in color) at each sensor as measured for IMB1 (left, a, c, e) and IMB2 (right, b, d, f). Colored lines indicate the detected material interfaces (air-snow interface in blue, ice surface and bottom in black and thermistor string plateau in red). The purple arrow points to the warming at the snow/ice interface, indicating flooding.
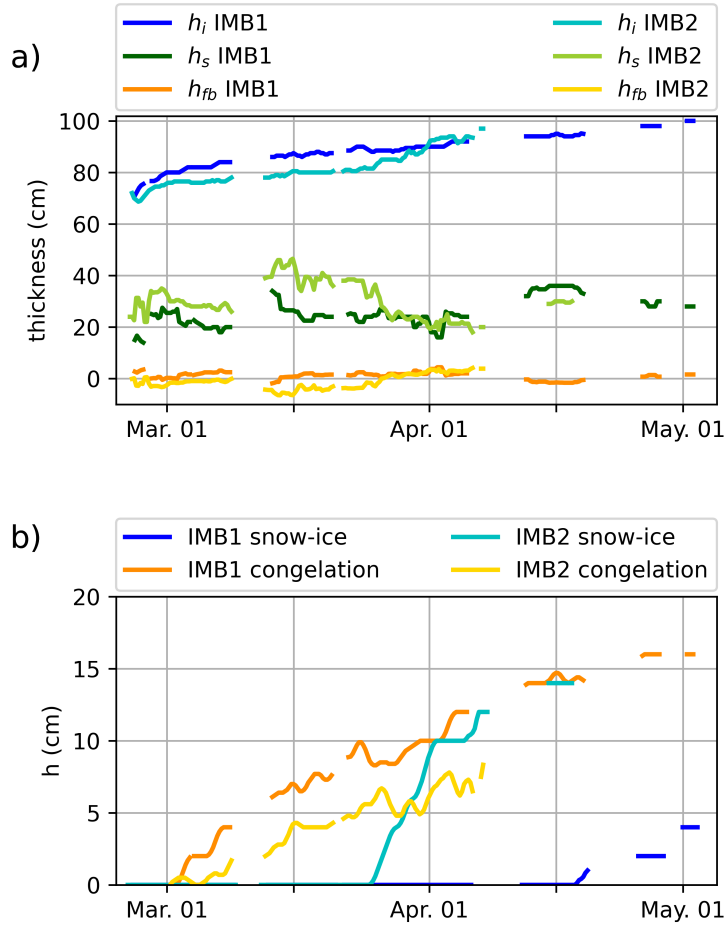
Figure 5. a) Ice (blue lines), snow (green lines), and freeboard (orange lines) thicknesses from the IMB observations. b) Contribution of snow-ice (blue lines) and congelation ice (orange lines) to the ice mass balance inferred from the IMB observations.
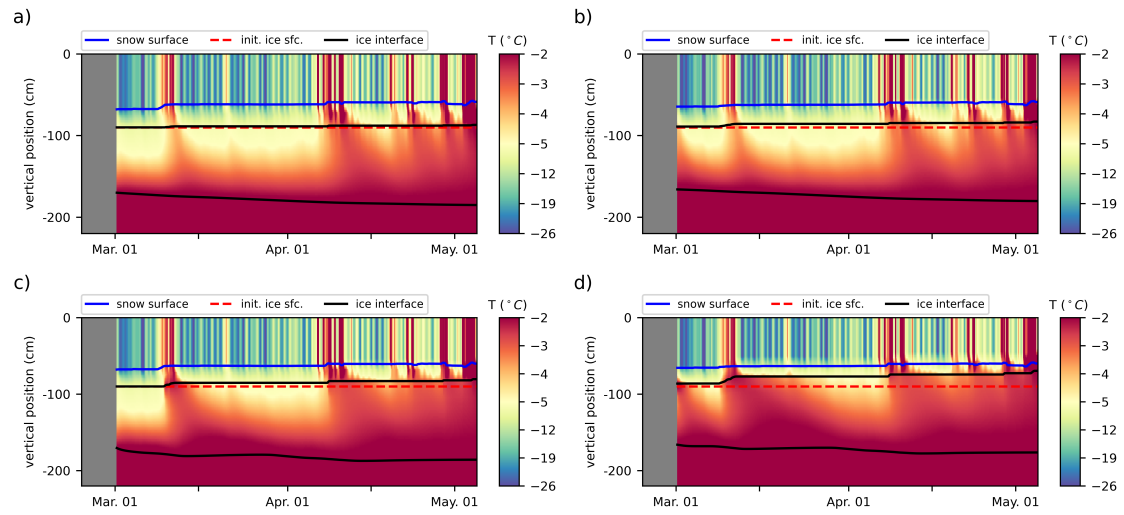
Figure 6. Simulated internal temperatures (color) interpolated into 2cm intervals from the BL99 (a,b) and mushy simulations (c, d), initialized from the IMB1 (a,c) and IMB2 (b, d) data. Solid lines indicate the simulated material interfaces (air-snow interface in blue, ice interfaces in black).
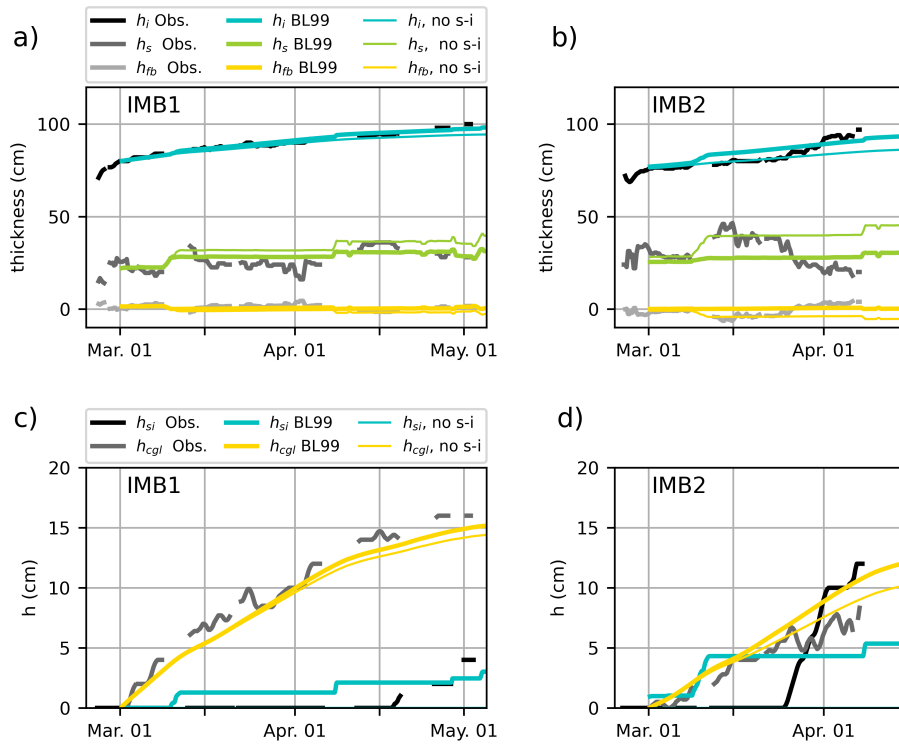
Figure 7. Ice mass balance in the BL99 simulations against the IMB1 (a,c) and IMB2 (b,d) observations. Top pannels (a,b): ice thickness (blue lines), now depth (green lines) and freeboard (yellow lines) values, with the IMB observations in black. Bottom pannels (c,d): cumulative ice growth from ice bottom (yellow lines) and snow-ice formation (blue lines), with the IMB observations in black. Thin lines indicate results from the BL99 simulation ran without using the snow-ice parameterization.
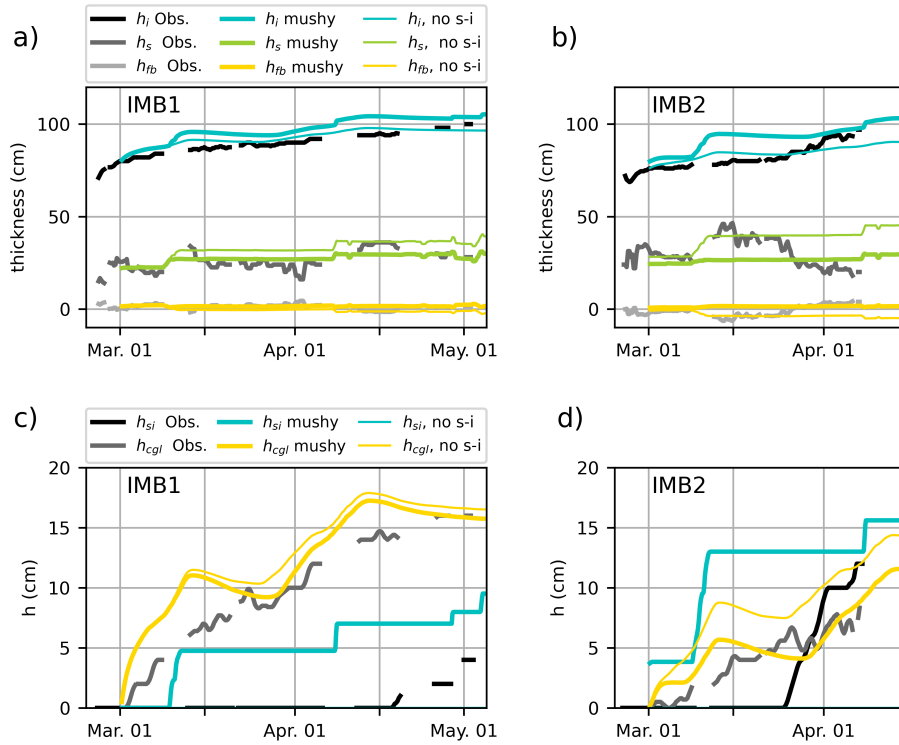
Figure 8. Ice mass balance in the mushy layer simulations against the IMB1 (a,c) and IMB2 (b,d) observations. Top pannels (a,b): ice thickness (blue lines), now depth (green lines) and freeboard (yellow lines) values, with the IMB observations in black. Bottom pannels (c,d): cumulative ice growth from ice bottom (yellow lines) and snow-ice formation (blue lines), with the IMB observations in black. Thin lines indicate results from the mushy simulations ran without using the snow-ice parameterization.
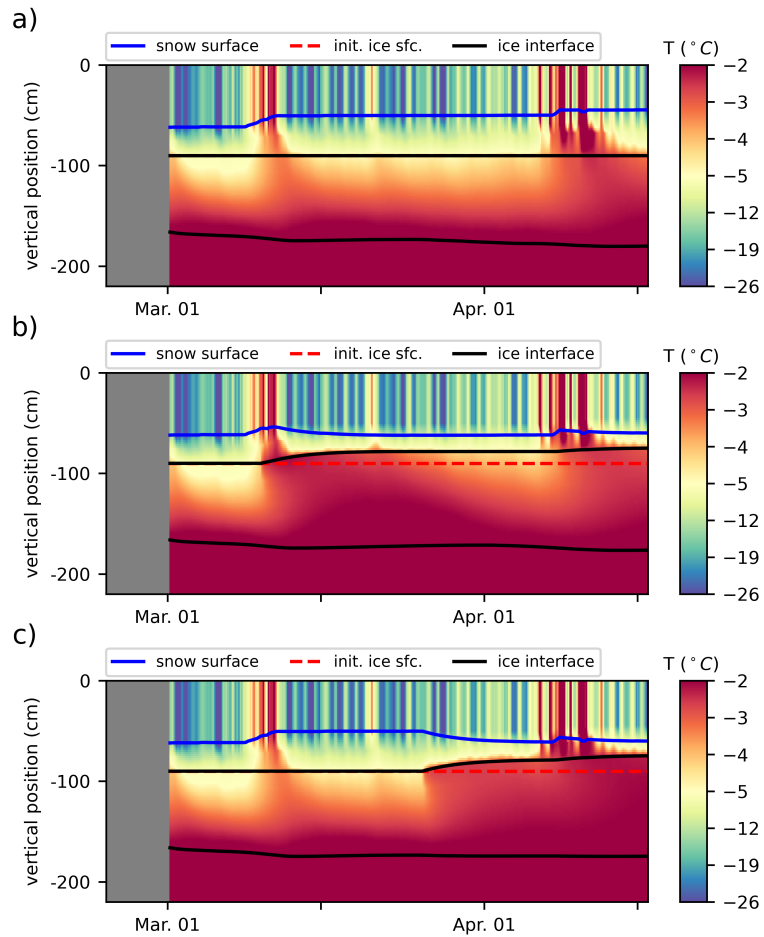
Figure 9. Time series of the simulated vertical temperature profiles (color), interpolated in 2 cm intervals to reproduce the IMB2 records, using the mushy layer physics with different criteria for snow flooding. Thick lines indicates the material interfaces (air-snow in blue, ice interfaces in black). a) Without snow flooding, b) using ϕ= 0.005 as a snow flooding onset criteria and c) manually setting the snow flooding onset on March 26th to match the observations.
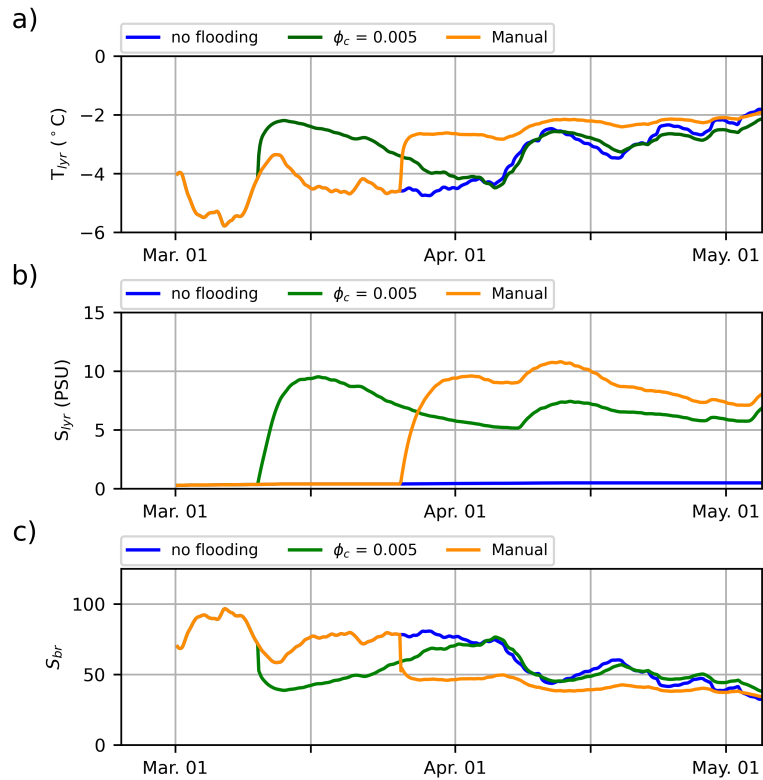
Figure 10. Time series of the (a) temperature, (b) bulk salinity and (c) brine salinity in the upper ice layer, in mushy simulations with different criteria for snow-ice formation (blue lines: no flooding).
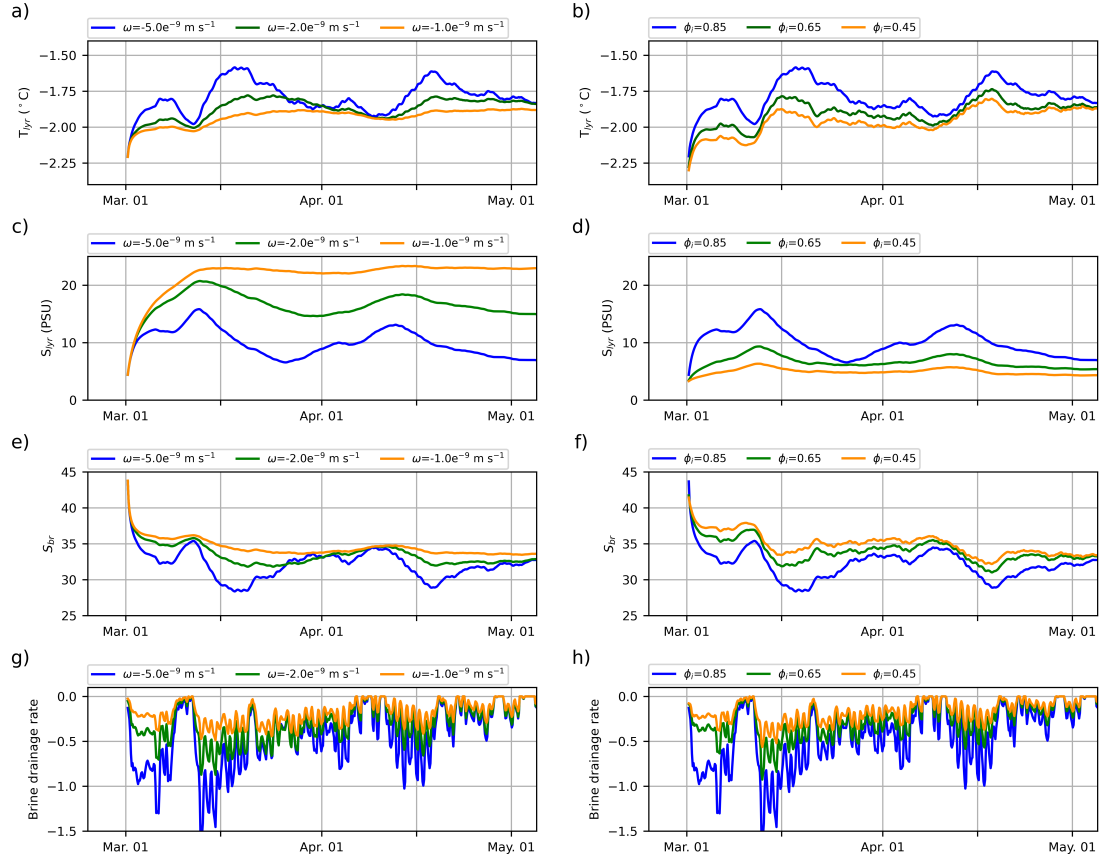
Figure 11. Time series of the (a,b) temperature, (c,d) bulk salinity, (e,f) brine salinity and (g,h) desalination rate from the slow brine drainage parameterization in the lowest ice layer, in mushy simulations with different brine drainage strength parameters (and standard congelation, left column) and different initial congelation liquid fraction ϕ_{init} (modified congelation, right column).
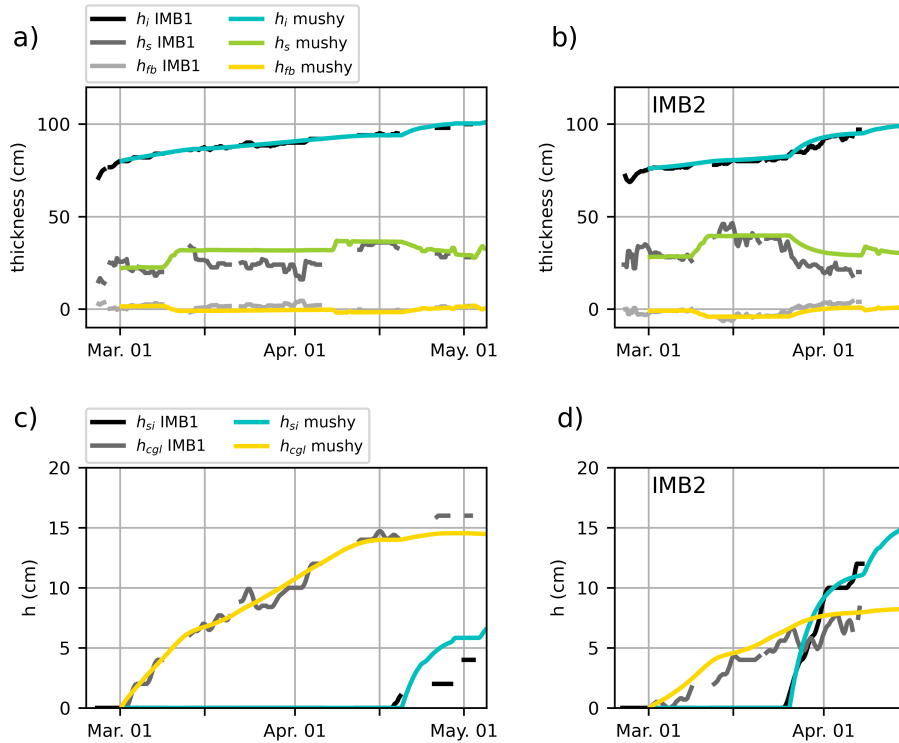
Figure 12. Ice mass balance in the mushy layer simulations tuned to best represent the observations, against the IMB1 (a,c) and IMB2 (b,d) records (in black). The snow flooding onset is set manually according to the observed flooding onset dates, and the simulations use the modified congelation scheme with ϕ_{init}=0.45. Top pannels (a,b): ice thickness (blue lines), now depth (green lines) and freeboard (yellow lines) values, with the IMB observations in black. Bottom pannels (c,d): cumulative ice growth from ice bottom (yellow lines) and snow-ice formation (blue lines), with the IMB observations in black.
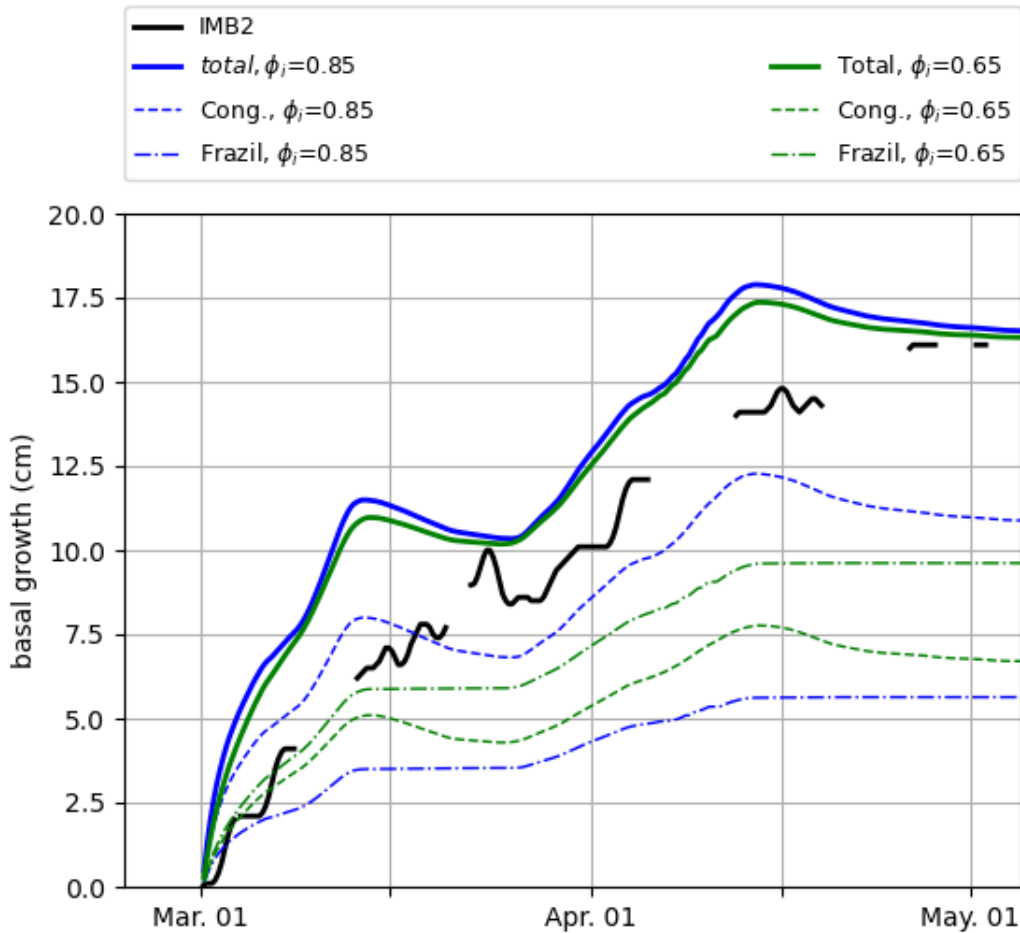
Figure 13. Total basal ice growth (solid lines) and contributions from congelation (dashed lines) and frazil formation (dot-dashed lines) in mushy simulations using the standard congelation scheme, with different initial congelation liquid fraction: default ϕ_{init}=0.85 in blue, ϕ_{init}=0.65 in green.
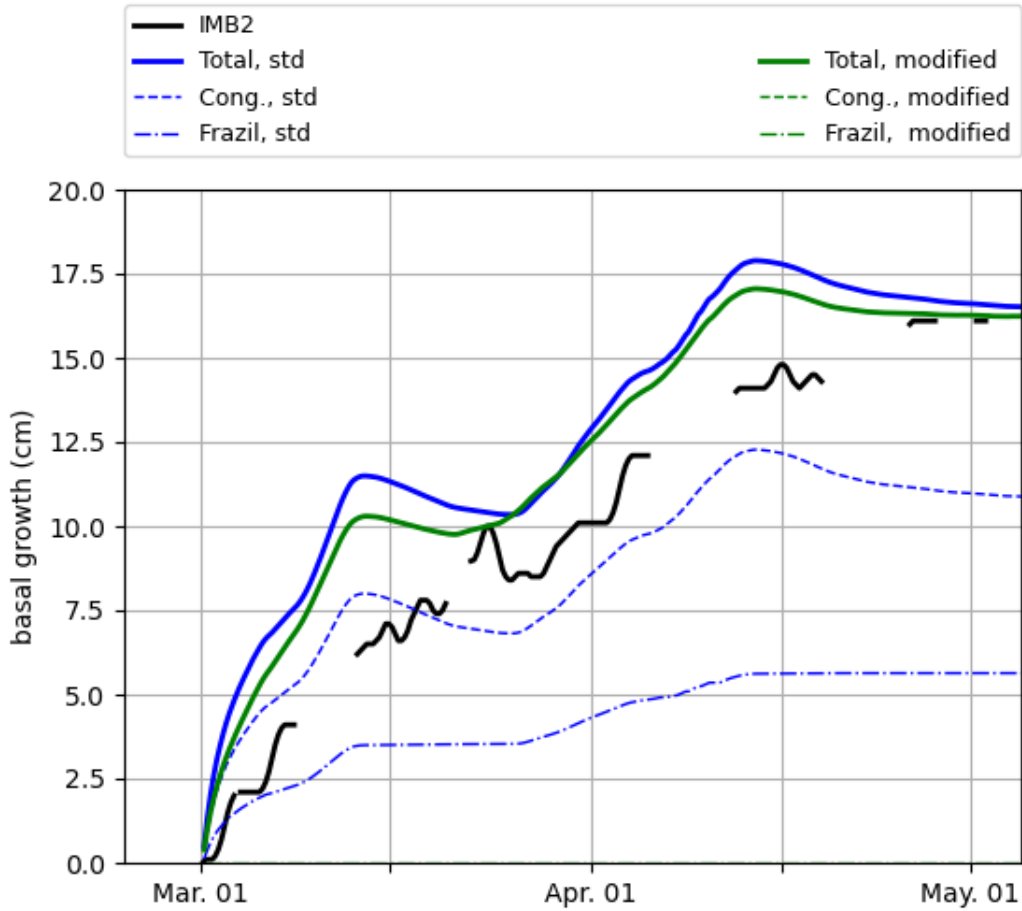
Figure 14. Total basal ice growth (solid lines) and contributions from congelation (dashed lines) and frazil formation (dot-dashed lines) in mushy simulations using the standard (blue) and modified (green) congelation schemes, both with default ϕ_{init}=0.85. Using the modified congelation scheme, the total basal growth and congelation lines are superposed as the frazil formation is zero.
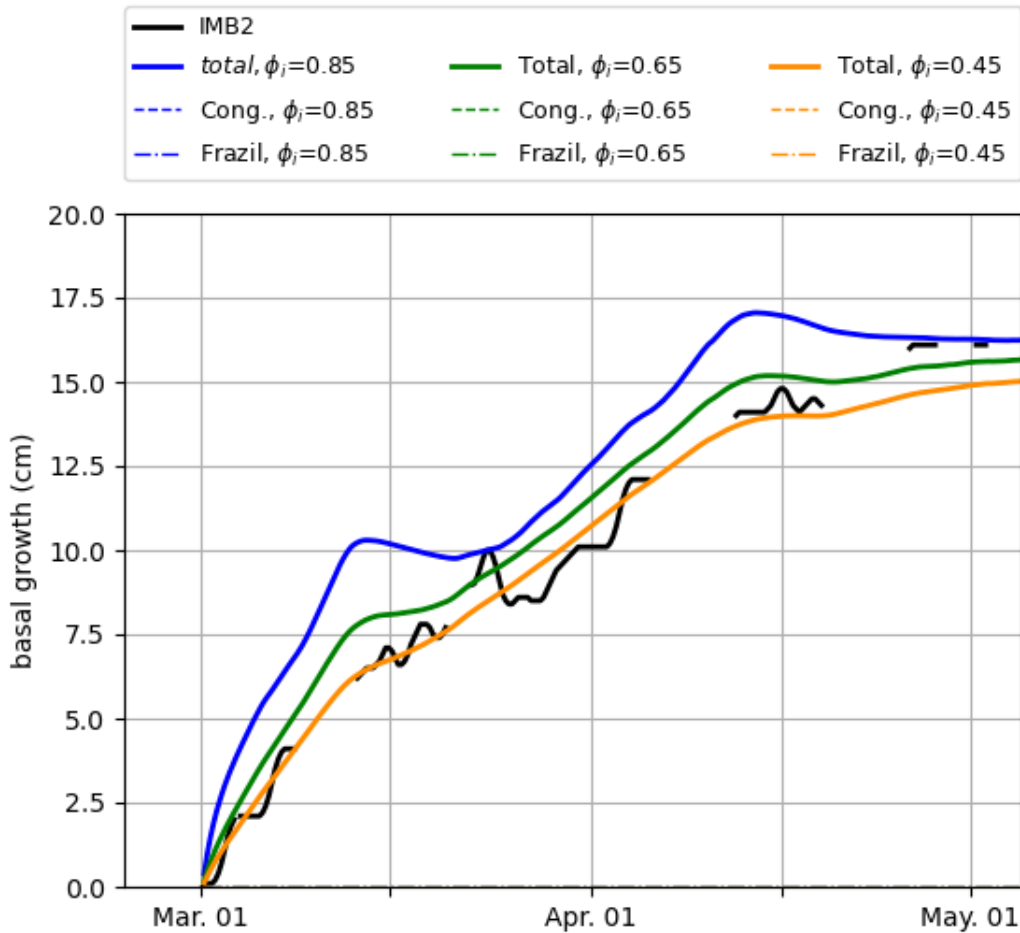
Figure 15. Total basal ice growth (solid lines) and contributions from congelation (dashed lines) and frazil formation (dot-dashed lines) in mushy simulations using the modified congelation scheme, with different initial congelation liquid fraction. The total basal growth and congelation lines are superposed as the frazil formation is zero.